MICROWAVE RESONANT SENSOR INTEGRATION WITH IMPEDANCE CYTOMETRY IN MICROFLUIDIC PLATFORM FOR PROBING MICRO-SCALE DIELECTRIC PERMITTIVITY

A THESIS SUBMITTED TO

THE GRADUATE SCHOOL OF ENGINEERING AND SCIENCE

OF BILKENT UNIVERSITY

IN PARTIAL FULFILLMENT OF THE REQUIREMENTS FOR

THE DEGREE OF

MASTER OF SCIENCE

IN

MECHANICAL ENGINEERING

By

Uzay Tefek

September 2023

Microwave Resonant Sensor Integration with Impedance Cytometry in Microfluidic Platform for Probing Micro-Scale Dielectric Permittivity
By Uzay Tefek
September 2023

We certify that we have read this thesis and that in our opinion it is fully adequate, in scope and in quality, as a thesis for the degree of Master of Science.

Assoc. Prof. Mehmet Selim Hanay(Advisor)

Prof. Alper Demir

Asst. Prof. Yegan Erdem

Approved for the Graduate School of Engineering and Science:

Orhan Arıkan
Director of the Graduate School

ABSTRACT

MICROWAVE RESONANT SENSOR INTEGRATION WITH IMPEDANCE CYTOMETRY IN MICROFLUIDIC PLATFORM FOR PROBING MICRO-SCALE DIELECTRIC PERMITTIVITY

Uzay Tefek
M.S. in Mechanical Engineering
Advisor: Assoc. Prof. Mehmet Selim Hanay
September 2023

This thesis presents a novel multiphysical sensor that integrates low-frequency impedance cytometry with high-frequency microwave capacitance sensing. The characterization of microscale objects, including microparticles and cells, is essential in various scientific disciplines, such as biology, materials science, and environmental science. Accurate identification and classification of these microscale entities are critical for applications ranging from drug delivery optimization to environmental impact assessment, however, the current techniques fall short in terms of the rapidity and cost-effectiveness necessary for analyzing extensive populations. To address this challenge, our hybrid sensor combines low-frequency impedance cytometry and high-frequency microwave capacitance sensing for material characterization based on dielectric permittivity. This integration offers a rapid, cost-effective, and highly accurate method for identifying and characterizing microscale particles and cells. Experimental studies demonstrate the sensor's efficacy, achieving remarkable signal-to-noise ratios. The sensor's versatility extends monitoring permittivity changes in single cells exposed to fixing agents offering valuable insights into cellular properties. In summary, this thesis introduces an innovative multiphysical sensor that advances microscale entity analysis, enabling rapid and precise identification and characterization.

Keywords: Impedance Cytometry, Microwave Sensors, Microplastics, Microparticles, Dielectric Characterization, Microwave Resonators, Clausius-Mossotti Factor.

ÖZET

MİKRO ÖLÇEKTE DİELEKTRİK GEÇİRGENLİĞİ İNCELEMEK İÇİN MİKROAKIŞKAN PLATFORMDA EMPEDANS SİTOMETRİ İLE MİKRODALGA REZONANS SENSÖRÜNÜN ENTEGRASYONU

Uzay Tefek
Makine Mühendisliği, Yüksek Lisans
Tez Danışmanı: Assoc. Prof. Mehmet Selim Hanay
Eylül 2023

Bu tez, düşük frekanslı empedans sitometrisini mikrodalga frekanslarında çalışan kapasitans algılama sensörüyle entegre ederek ortaya çıkan yeni bir sensör sunmaktadır. Mikropartiküller ve hücreler de dahil olmak üzere mikro ölçekli nesnelerin karakterizasyonu; biyoloji, malzeme bilimi ve çevre bilimi gibi çeşitli bilimsel disiplinlerde gerek duyulmaktadır. Bu mikro ölçekli varlıkların doğru tanımlanması ve sınıflandırılması, ilaç dağıtım optimizasyonundan çevresel etki değerlendirmesine kadar çeşitli uygulamalar için kritik önem teşkil etmektedir, ancak mevcut teknikler, geniş popülasyonları analiz etmek için gereken hız ve maliyet etkinliği açısından yetersiz kalmaktadır. Bu zorluğun üstesinden gelmek için hibrit sensörümüzde, dielektrik geçirgenliğe dayalı malzeme karakterizasyonu yapabilmek için iki farklı frekansta çalışan sensörü birleştirildi. Bu entegrasyon, mikro ölçekli parçacıkların ve hücrelerin tanımlanması ve karakterize edilmesi için hızlı, uygun maliyetli ve son derece doğru bir yöntem sunar. Deneysel çalışmalar, sensörün etkinliğini ve dikkate değer sinyal-gürültü oranlarına ulaştığını göstermektedir. Sensörün uygulama çeşitliliğine örnek olarak hücre sabitleme işlemine maruz kalan tek hücrelerdeki elektrik alan geçirgenliği değişikliklerinin izlenmesiyle hücreselin içsel özellikleri hakkında bilgi edinilebilmesi verilebilir. Özetle, bu tez, mikro ölçekli varlıkların analizini geliştiren, hızlı ve doğru tanımlama ve karakterizasyona olanak tanıyan yenilikçi bir çoklu fiziksel sensör sunmaktadır.

Anahtar sözcükler: Empedans Sitometri, Mikrodalga Sensörleri, Mikroplastikler, Mikropartiküller, Dielektrik Karakterizasyon, Mikrodalga Rezonatörler, Clausius-Mossotti Faktörü.

Acknowledgement

I am profoundly grateful to my advisor, Assoc. Prof. Selim Hanay, for his unwavering support and guidance throughout my undergraduate and master's programs. His expertise and creative way of thinking have always been invaluable to me and have played a crucial role in the success of this thesis. In fact, he is one of the major reasons why I chose to study mechanical engineering at Bilkent. When I graduated from high school, I came across his research projects and was immediately drawn to the intriguing nature of his work. Now, here I am, sharing the pride of having contributed to the research of such an amazing supervisor.

I would also like to extend my gratitude to Prof. Alper Demir and Asst. Prof. Yegan Erdem for their contributions to my thesis committee.

Sincere thanks go to my family for their unwavering support, belief in me, and everything they have done for me. I have always felt their unconditional love, which has empowered me throughout my life.

I am thankful to my girlfriend, Çiğdem Çelebi, for always being my safe haven. She is consistently one step ahead of me, looking out for my well-being. I consider myself incredibly lucky to have such an amazing person in my life.

I want to express my appreciation to the members of the Hanay Research Group: Batuhan Emre Kaynak, Sayedus Salehin, Yağmur Ceren Alataş, Mohammed Alkhaled, and Enise Kartal for their valuable discussions and collaboration. I'd like to give special thanks to Hashim Alhmoud for being like a big brother to me. Beyond your deep knowledge and excellent academic expertise, I know I can count on you for anything. I'd also like to express my gratitude to the alumni members of the Hanay Group, including Arda Seçme, Berk Küçükoğlu, Mehmet Kelleci, Tufan Erdoğan, Berke Demiralp, Mert Yüksel, Utku Hatipoglu, Hande Aydogmus, Selcuk Erbil, and Levent Aslanbas, for teaching and guiding me throughout this journey.

A special thanks go to Burak Sarı, my friend, teacher, and late-night experiment companion, 'dayı'. He was the perfect lab partner for me who was always patient and enthusiastic about teaching. He is one of the top people one could listen to for hours. Without him, this work would not have been possible.

I would also like to thank my friends from the graduate office, Sena Pekol, Berkay Şahinoğlu, Özgür Can Gümüş, Emirhan İnanç, Abdullah Habboush, Aykut Bakan, Alihan Bakır, Doğa Dağ, and Yusuf Uzun, for making the office an enjoyable place.

This project has received funding from the European Research Council (ERC) under the European Union's Horizon 2020 research and innovation programme (grant agreement No 758769).

Contents

List of Figures

Chapter 1

Introduction

The characterization of microscale objects has emerged as a crucial area of research with broad implications across various scientific disciplines, including biological, materials, and environmental sciences. Accurate identification and classification of microscale particles, such as microparticles and cells, are essential for understanding biological processes, optimizing drug delivery systems, and assessing environmental impact [1, 2]. In the field of biomedical applications, differentiation of cell types is crucial for various diagnostic and therapeutic purposes [3, 4]. High-throughput techniques are needed to efficiently classify cells and assess their responses to external stimuli or drug treatments [5]. Moreover, in materials science, the optimization of drug loading efficiency in micropolymer-based formulations can enhance the effectiveness of medications and reduce production costs. In environmental screening, the increasing concerns about the environmental impact of industrial microparticles, particularly in the context of microplastic pollution, require robust methods for their detection and characterization.

There are several well-established analytical techniques for the identification and classification of microscale particles. Techniques like Raman and Fourier Transform Infrared Spectroscopy (FTIR) are powerful tools for detailed material characterization. While these methods are accurate and widely used in research laboratories, they suffer from certain limitations when applied to microparticle

analysis. Raman and FTIR require bulky and expensive instrumentation and are often time-consuming for the analysis of large particle populations [6, 7]. In an interlaboratory study dedicated to finding out the most effective methods for microplastic characterization in drinking water, the average time spent on Raman is 10 minutes and on FTIR 12 minutes per particle [7]. Additionally, for the particle size below 20 μm, which is particularly important concerning human exposure and health effects, [8] these techniques struggle to achieve high-accuracy results due to their relatively weak scattering signals.

An alternative technique, impedance cytometry, has shown promise for the rapid sizing of microparticles and cells. Impedance cytometry operates by detecting the change in ionic current when an analyte dielectric particle blocks the current flow between two electrodes with a potential difference. At lower frequencies (¡1 MHz), impedance cytometry can size microparticles based on their geometric volume. However, this technique lacks the capability to differentiate between different materials effectively [9]. The real challenge lies in classifying microparticles based on their material composition, especially when they have similar geometric sizes.

Researchers have explored various strategies to address this challenge and improve impedance cytometry with material characterization capabilities. One approach involves employing higher radio frequencies (typically 1 to 50 MHz) where the capacitive response of dielectric particles can provide information about their electrical permittivity [10]. At these frequencies, the capacitive impedance of the cell membrane becomes small compared to the cytosol, allowing for the probing of internal cellular parameters. This method has been successfully applied to differentiate biological cells from non-biological microparticles, thanks to the high water content of cells, which imparts a distinct dielectric response.

However, differentiating non-biological microparticles from one another in water remains a formidable challenge due to the high polarizability of water and ions dissolved in it. At low frequencies, the electrical response is mainly dependent on particle volume, and any material-based information is overwhelmed by the presence of water [11]. To overcome this limitation, researchers have explored

the application of microwave resonators operating at frequencies in the low GHz range (1-20 GHz) [12, 13, 14, 15, 16, 17, 18, 19, 20]. At these frequencies, ion screening effects are diminished, and electrical response primarily reflects the inherent properties of the particle's material.

Microwave resonators offer several advantages for microparticle analysis. Firstly, they provide non-contact measurements through integrated antennas, enabling precise detection without direct contact with the analyte. This feature is particularly valuable when handling delicate biological cells. Secondly, the small form factor and compactness of microwave resonators make them ideal candidates for portable and point-of-care applications. Thirdly, researchers can leverage metamaterial approaches to engineer subwavelength structures, tuning the sensor response and enhancing its sensitivity and selectivity [21, 16].

This thesis presents a novel, multiphysical sensor that combines low-frequency (500 kHz) impedance cytometry with high-frequency (5 GHz) microwave capacitance sensing. The integration of these two distinct sensors provides complementary parameters for the rapid identification and characterization of microscale particles. The impedance cytometry sensor primarily detects the geometric volume of particles passing through the microfluidic channel [22]. On the other hand, the microwave sensor yields the capacitance, which is a function of both the geometric size and the Clausius-Mossotti factor, related to the particle's electrical permittivity.

We demonstrate the efficacy of our hybrid sensor through experimental studies focusing on the classification of polystyrene and soda-lime glass microparticles, both approximately 20 μm in diameter. Despite the low intrinsic contrast of these microparticles, our sensor achieves impressive signal-to-noise ratios (SNR) in microwave measurements (¿ 800) and low-frequency current measurements (600). The analysis of these high-resolution data sets reveals that the ratio of Clausius-Mossotti factors of the two microparticles is calculated to be 1.09, closely aligned with the theoretical value of 1.10. Moreover, our sensor achieves a remarkable accuracy of 94.9% in identifying particle materials, showcasing its potential for environmental screening and materials analysis. Furthermore, we demonstrate

the versatility of our sensor by investigating its utility in biomaterial and bioelectronics research. Specifically, we monitor the relative permittivity changes of single cells exposed to glutaraldehyde, a cellular fixing reagent. The result of this experiment highlights the potential of our sensor in cellular studies.

In short, this thesis introduces a novel multiphysical sensor that represents a significant advancement in microscale entity analysis, providing a rapid, cost-effective, and highly accurate method for identification and characterization. By integrating low-frequency impedance cytometry with high-frequency microwave capacitance sensing, we offer a unique platform for material differentiation based on dielectric permittivity, overcoming the limitations of existing techniques and opening up exciting opportunities for applications in environmental science, personalized medicine, and beyond.

Chapter 2

Theory of Operation

The Theory of Operation chapter serves as the theoretical foundation for the multiphysical sensor presented in this thesis. This chapter explains the two all-electronic sensing techniques employed by the sensor, namely Microwave Frequency Sensing and Low-Frequency Sensing. These complementary techniques provide crucial insights into the identification and characterization of microscale particles based on their dielectric permittivity.

In the first subsection, Microwave Frequency Sensing, we delve into the sensor modeling and its underlying principles. At microwave frequencies in the GHz range, the sensor exploits the capacitance changes induced by the interaction of microparticles with the electromagnetic field. A key parameter of interest in this context is the Clausius-Mossotti Factor, which is related to the dielectric permittivity of the particles. We explore how this factor is determined from the measured sensor response and how it forms the basis for material differentiation.

The second subsection, Low-Frequency Sensing, provides complementary information on the analyzed microparticles. This method operates at frequencies in the order of 500 kHz and utilizes impedance cytometry to detect the geometric volume of the particles passing through the microfluidic channel. We investigate two different designs for this low-frequency measurement, each offering distinct

advantages and applications.

2.1 Microwave Frequency Sensing

The study of particle sensing through electrical sensors is a well-established domain, especially in applications like biological sample sizing and sorting, often employing techniques like flow cytometry, sometimes incorporating optical measurement systems [12, 13, 14, 15, 16, 17, 18, 19, 20]. Many of these systems typically operate within the frequency range of a few hundred megahertz (MHz). However, delving into frequencies lower than the microwave spectrum (i.e., below 1 gigahertz or GHz) imposes limitations on our ability to access crucial information contained within particles and cells. These limitations stem from two key factors: the phenomenon of Debye screening by ion interfaces and the polarization of cellular membranes [23].

Microwave frequencies offer an intriguing solution to this challenge, as they present a scenario where ions within particles or cells struggle to respond swiftly to rapidly changing electrical fields, thus failing to impede the penetration of these fields. This phenomenon underscores the vital role of microwave frequencies when it comes to extracting content-related insights during the classification of particles and cells. Given the central focus of this thesis on the classification of particles and cells, primarily based on permittivity and content, microwave resonators are the instrumental choice for carrying out sensing operations within this frequency range.

Microwave resonator structures effectively store energy in the form of electric and magnetic fields and are characterized by the occurrence of resonance phenomena, driven by the presence of standing waves that they can support. The precise resonance frequency of these structures depends intricately on factors such as the material used and the geometry they exhibit. These structures also create localized electric and magnetic fields, which become indispensable components for facilitating sensing tasks. To further our understanding, we will embark on a

journey through a simplified model, starting with how the mere presence of a particle can introduce changes in capacitance within a microchannel. This seemingly subtle modification in capacitance will ultimately manifest itself in the signals we measure. Notably, the microwave sensor we employ in this research operates in the capacity of a capacitance sensor, bearing a resemblance to its counterparts in the realm of impedance spectroscopy. However, it does so within a notably higher frequency range, spanning from 4 to 8 GHz.

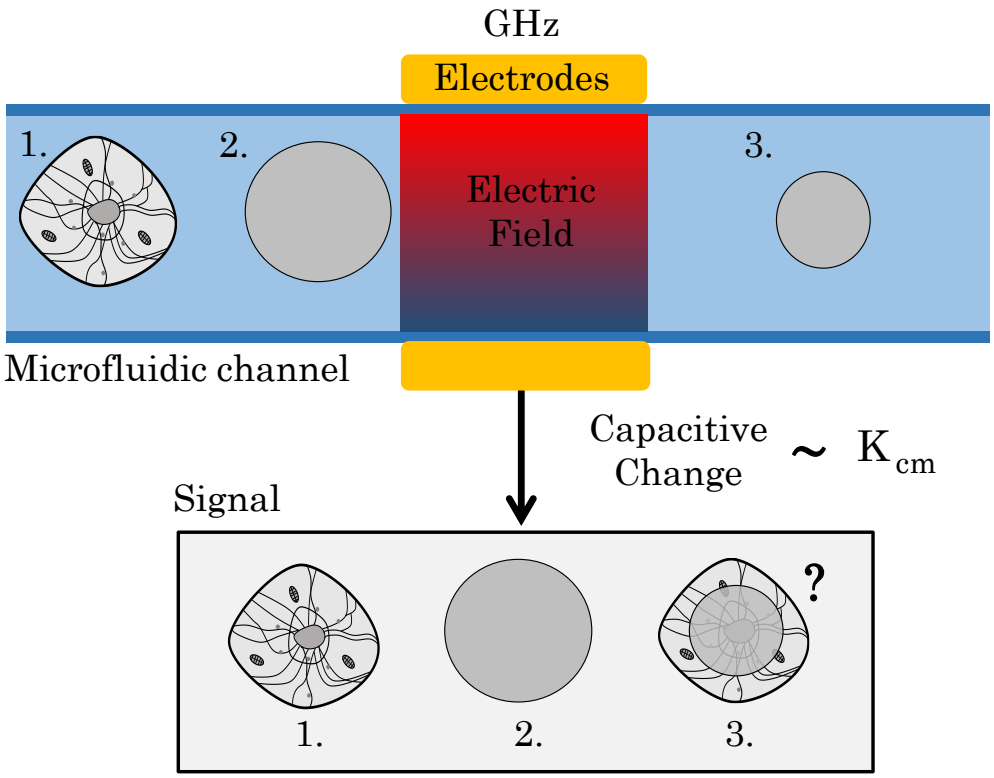

Figure 2.1: At Microwave Frequencies electric field is unaffected by Debye screening and can pass through the microparticle.

2.1.1 Out-of-Phase Component

The sensor's microwave behavior is represented by a series RLC circuit, wherein the passage of particles through the microchannel results in a change in capacitance (ΔC) [24]. In this type of circuit, the system's response can be described

by a transfer function in the frequency domain.

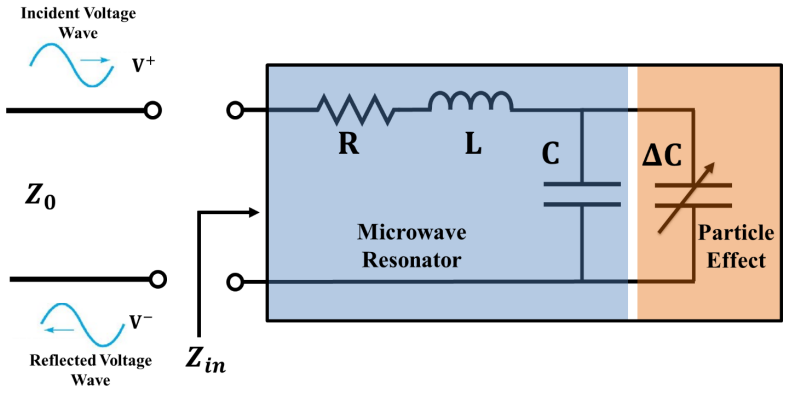

Figure 2.2: For the microwave resonator, particle passage in the microchannel can be modeled as a capacitance change of ΔC to the RLC circuitry

For our specific design, a single port Split Ring Resonator (SRR), this transfer function indicates the ratio of the reflected wave voltage (V-) to the incident wave voltage (V+), which is referred to as the S_{11} parameter. This parameter is influenced by both the line impedance of the measurement circuitry and the input impedance of the device (Z_{in}).

$$H(\omega) = \frac{V^-}{V^+} = S_{11} = \frac{Z_{in} - Z_0}{Z_{in} + Z_0} \tag{2.1}$$

For and RLC circuit the transfer function can be written as,

$$H(\omega) = \frac{(R - Z_0) + j(\omega L - \frac{1}{\omega(C+\Delta C)})}{(R + Z_0) + j(\omega L - \frac{1}{\omega(C+\Delta C)})} \tag{2.2}$$

Since the sensor is always driven at its resonance frequency, the impedance of the sensor has to be purely real. Therefore, at resonance.

$$\omega_{\text{res}} L - \frac{1}{\omega_{\text{res}} C} = 0 \tag{2.3}$$

Also, if use Taylor Expansion to the capacitance term to the first degree;

$$\frac{1}{\omega_{\text{res}}(C + \Delta C)} = \frac{1}{\omega_{\text{res}} C} - \frac{\Delta C}{\omega_{\text{res}} C^2} \tag{2.4}$$

Then, the transfer function at resonance frequency can be written as;

$$H(\omega_{\text{res}}) = \frac{(R - Z_0) + j\frac{1}{\omega_{\text{res}}}\left(\frac{\Delta C}{C^2}\right)}{(R + Z_0) + j\frac{1}{\omega_{\text{res}}}\left(\frac{\Delta C}{C^2}\right)} \tag{2.5}$$

If the expression is multiplied with its complex conjugate and its real and imaginary parts are separated;

$$\text{Re}\{H(\omega_{\text{Res}})\} = \frac{R^2 - Z_0^2 + \frac{1}{\omega_{\text{res}}^2}(\frac{\Delta C}{C^2})^2}{(R + Z_0)^2 + \frac{1}{\omega_{\text{res}}^2}(\frac{\Delta C}{C^2})^2} \tag{2.6}$$

$$\text{Im}\{H(\omega_{\text{Res}})\} = \frac{\frac{2Z_0}{\omega_{\text{res}}}(\frac{\Delta C}{C^2})}{(R + Z_0)^2 + \frac{1}{\omega_{\text{res}}^2}(\frac{\Delta C}{C^2})^2} \tag{2.7}$$

The capacitance change is going to reflect itself to the first order in the out-of-phase component (i.e., the imaginary part of the transfer function), but the second order in the in-phase component (i.e., the real part of the transfer function). Furthermore, $\Delta C \ll C$ which means $(\Delta C/C^2)^2 \ll 1$, and the imaginary part can be simplified as;

$$\Delta Y = \text{Im}\{H(\omega_{\text{Res}}, \Delta C)\} = \frac{\frac{2Z_0}{\omega_{\text{res}}C}}{(R + Z_0)^2}\left(\frac{\Delta C}{C}\right) \tag{2.8}$$

Since the terms Z_0, ω_{Res}, C and R are constant during the experiment, we can finally end up with the following relation;

$$\Delta Y \propto \Delta C \tag{2.9}$$

By employing the equations 2.10 and 2.9, we aim to determine the Clausius-Mossotti factor for micro-objects using a microwave resonant sensor.

2.1.2 Clausius-Mossotti Factor

The Clausius-Mossotti factor, denoted as K_{CM}, is a pivotal parameter within the realm of dielectric materials and plays a fundamental role in understanding their response to electric fields. This factor is instrumental in the context of our sensor technology and is integral to elucidating the behavior of micro-scale particles and cells.

The Clausius-Mossotti factor quantifies the polarizability of a material when subjected to an external electric field. It is defined as:

$$K_{CM} = \frac{\varepsilon - \varepsilon_m}{\varepsilon + 2\varepsilon_m}$$

Where: - ε represents the dielectric constant (permittivity) of the material under study. - ε_m denotes the dielectric constant of the surrounding medium.

This factor is of particular importance as it provides insights into how a material's dielectric properties change when exposed to an electric field. It is crucial to understand phenomena such as polarization and how our sensor measures these changes.

The value of the Clausius-Mossotti factor influences the extent of polarization a material undergoes when placed in an electric field. A positive value of K_{CM} implies that the material polarizes in the same direction as the applied field, while a negative value indicates polarization in the opposite direction. Moreover, the magnitude of K_{CM} offers insights into the degree of polarization.

In the context of our experiments, the Clausius-Mossotti factor serves as a key parameter in interpreting the sensor's response to micro-scale particles and cells. It aids in understanding how these entities influence the dielectric properties of the medium they are suspended in, allowing us to differentiate and characterize them effectively.

In the Experimental Results sections, we delve into specific experiments where the Clausius-Mossotti factor plays a pivotal role in our analysis. It enables us to establish the relation between our sensor readings and micro-objects' dielectric properties with the following equation:

$$\Delta C = 4\pi\varepsilon_m a^3 K_{CM} |E_{rms}|^2 U^2 \tag{2.10}$$

Where C is capacitance, ε_m is the dielectric permittivity of the medium, a is particle radius, E_{rms} is the magnitude of the root mean squared (RMS) electric field and U is electrical potential. In line with this equation, the alteration in capacitance also hinges on the physical size of the micro-object under examination, introducing an element of uncertainty. It's important to note that an identical change in capacitance can be triggered by either a small particle with a high K_{CM} value or a larger cell with a comparatively lower K_{CM} value, as illustrated in Figure 2.3. Consequently, relying solely on microwave frequency sensing, we encounter a challenge in precisely pinpointing the nature of what we are measuring.

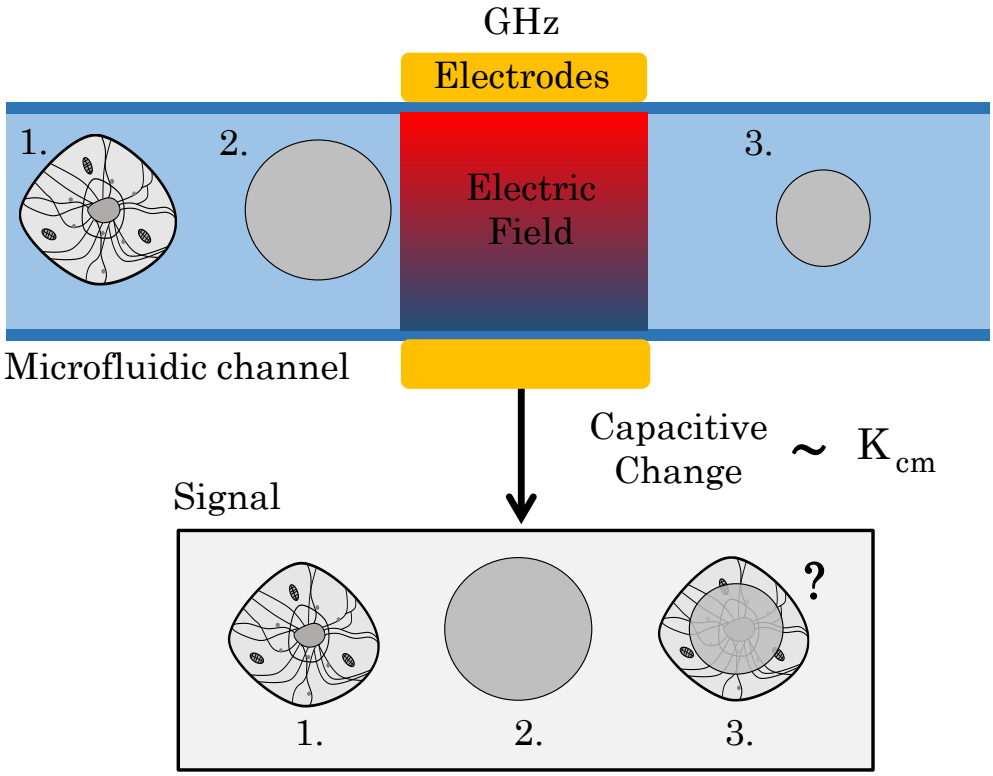

Figure 2.3: At Microwave Frequencies electric field is unaffected by Debye screening and can pass through the microparticle.

2.2 Low Frequency Sensing

Impedance cytometry is a powerful analytical technique employed in the realm of biophysics and cellular analysis [25]. It stands as a versatile and informative method for characterizing cells, particles, and microorganisms based on their electrical properties. Unlike its microwave frequency counterpart, impedance cytometry operates within the low-frequency range, typically spanning from kilohertz (kHz) to megahertz (MHz). This technique capitalizes on the inherent electrical conductivity variations exhibited by different biological entities, offering valuable insights into their size.

At the heart of impedance cytometry lies the fundamental principle of measuring impedance, which is the opposition to the flow of alternating current (AC)

within a biological sample. This opposition stems from the resistive properties of the sample.

Impedance cytometry finds diverse applications across various fields, including counting and sizing. Impedance cytometry is extensively used to enumerate and size cells within a sample [26, 27, 28]. The technique is particularly valuable in clinical diagnostics, where it aids in monitoring blood cell counts, detecting abnormalities, and diagnosing diseases.

Beyond cellular applications, impedance cytometry is employed in the analysis of various particles and microparticles, including synthetic particles, nanoparticles, and microbeads [29]. It aids in characterizing their physical and electrical properties.

Impedance cytometry experiments typically involve a microfluidic system where the sample of interest is suspended in an electrolyte solution. The sample flows through a microchannel or chamber, and electrodes positioned at specific points within the channel measure the impedance changes as the sample passes through. The impedance data is then analyzed to extract relevant information about the cells or particles.

Impedance cytometry offers several advantages, including its label-free nature, rapid data acquisition, and the ability to analyze large cell populations. However, it has limitations. Since the electrical signal cannot probe into cells due to double layer occurrence and Debye shielding the technique becomes ineffective in providing detailed information about micro-object morphology (Figure 2.4 [30, 31].

In summary, impedance cytometry, operating within the low-frequency range, plays a crucial role in the field of cellular analysis and particle characterization. Its ability to discriminate between biological entities based on electrical properties has led to its widespread adoption in clinical, research, and industrial settings, making it a valuable tool for understanding cellular behavior and investigating micro-scale particles.

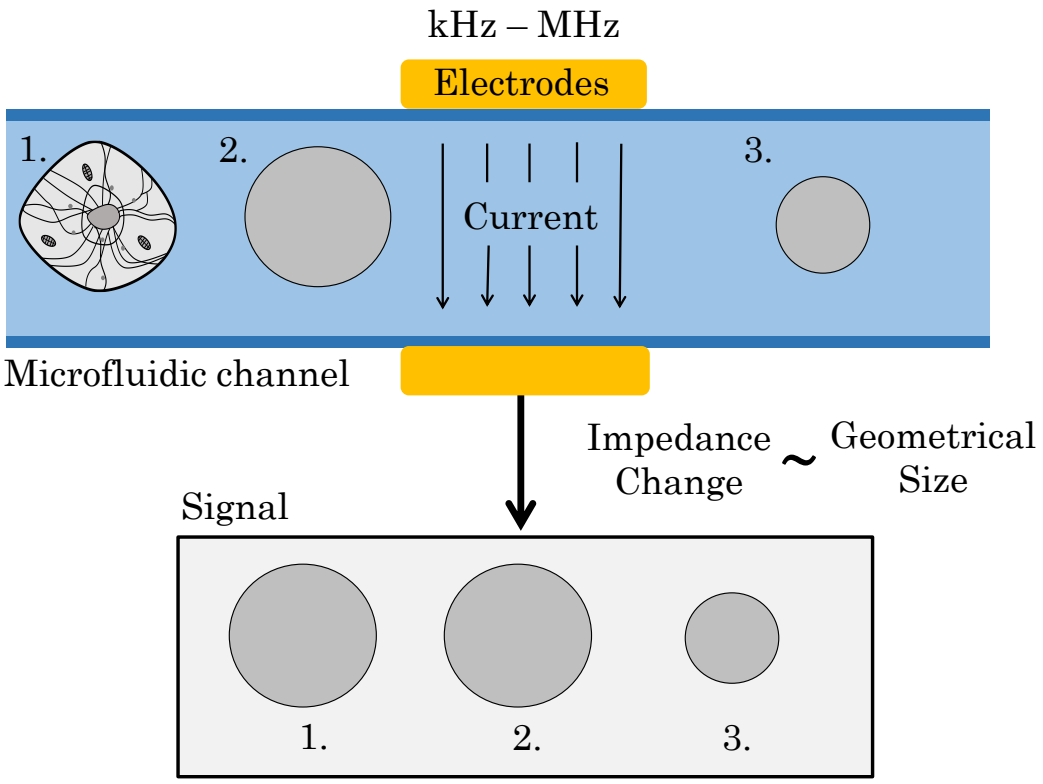

Figure 2.4: At kHz-MHz Frequency the electrical signal is transferred as electrical current. Any dielectric material blocks the current flow.

Chapter 3

Evolution of the Sensor Design

In the pursuit of accurate and efficient microscale particle analysis, the evolution of sensor design stands as a testament to the pursuit of innovation. This chapter delves into the complications of the sensor designs developed and modified over the course of this research, each representing a step forward in capturing the properties of microscale particles. Through a journey of experimentation, analysis, and modification; these sensor designs have been molded to overcome challenges, unlock new insights, and provide a comprehensive understanding of microparticle analysis.

The evolution of the sensor design chapter is not only a chronicle of technological advancements but also a narrative of the rigorous quest to enhance the precision, sensitivity, and applicability of microscale particle analysis. With each iteration, these sensor designs have been improved to target specific aspects of particle characterization, whether it be material composition, geometrical size, or error compensation methods. This chapter explains the distinctive characteristics and principles that underlie each sensor design, laying the foundation for a comprehensive understanding of their functioning and implications.

3.1 Microwave Sensor with Optical Imaging

The initial design I worked with was a Split-Ring Resonator with only one parallel electrode pair in the sensing region. A microfluidic channel with 250 μm width was chosen to ease the alignment of the PDMS block with the microwave electrodes. However, due to the limited coverage of the electric field between the electrodes across the channel width, there were fringing electric fields in both lateral and vertical directions. Consequently, particles passing close to the channel walls, where the electric field was most non-uniform, were excluded from the dataset. This reduced the throughput of the sensor. Moreover, since there was no mechanism to calculate the trajectory height of the particles, even among the particles passing through the middle section, the measured signal variance was quite high.

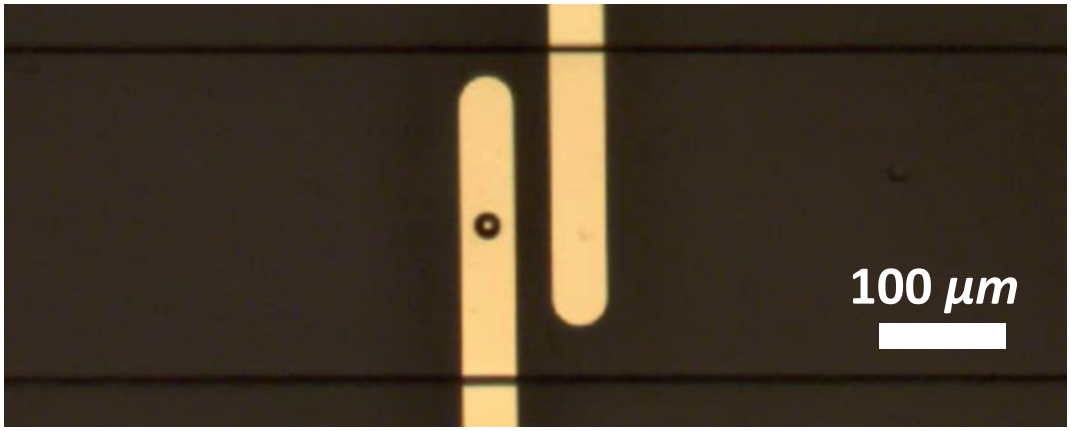

Figure 3.1: Sensing region of the microwave sensor with optical imaging. A parallel electrode pair with 30-μm gap in between is placed perpendicular to fluid flow.

For the dielectric permittivity measurement, a custom electronic setup was employed, comprising a signal generator, detection circuitry, and a controller. The controller utilized the phase change ($\Delta\omega$) of the resonator as an error signal to estimate the resonance frequency, which depended on the capacitance change. The phase change ($\Delta\theta$) was found to be proportional to the capacitance change (ΔC) for a given set of amplitude (R) and phase (θ), where N(R,θ) represented a normalization factor, constant during each experiment due to controller adjustments.

The output of the detection circuit, θ_{out}, provided the phase difference between the instantaneous phase and the reference phase at the resonance frequency of the device, serving as an error signal for the controller circuit. To address this error signal, a Proportional-Integrative (PI) controller was utilized. This PI controller generated a control signal ($\omega_{correction}$) and sent it to the signal generator through a LabView interface. The control signal updated the drive frequency of the microwave signal generator (ω_{drive}) until it matched the resonance frequency (ω_{res}) of the sensor. With this approach, the phase angle of the resonator response function was locked at 0 degrees, forming a Frequency-Locked Loop (FLL). Any deviation of the phase from 0 degrees emerged as an error signal, which was used to precisely update the frequency of the signal generator. Through this method, we were able to continuously track the resonance frequency changes as can be seen in Figure 3.2. [32]

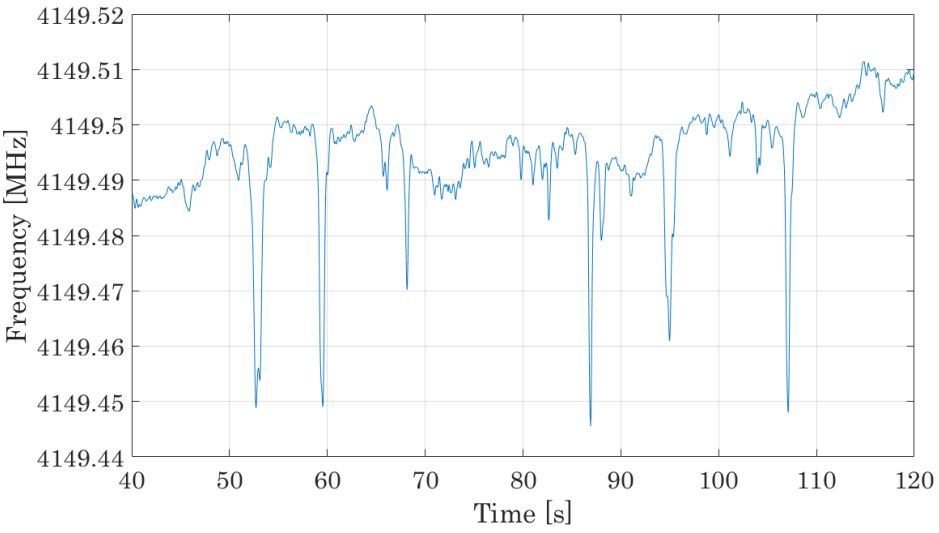

Figure 3.2: A section of the raw data. Using the phase-locked-loop controller, we detect the impact of passing microparticles through the sudden shift in the resonance frequency.

For the volume calculation of the microparticles, we used bright-field optical microscopy recordings to measure their diameters, assuming a spherical shape. During the experiment, the sensing region was recorded, and a custom image

processing code was implemented to detect the event frames. The image processing algorithm is initiated by using a video frame of the sensing region without any particle as a reference frame (Figure 3.3A). All the frame images were then converted to grayscale and stored as matrices. Each video frame's matrix (Figure 3.3B) was subtracted from the reference frame, and the summation of row and column values was plotted (Figure 3.3C). By applying a threshold to filter the summation results, we successfully captured all the event frames and matched them with the microwave signal.

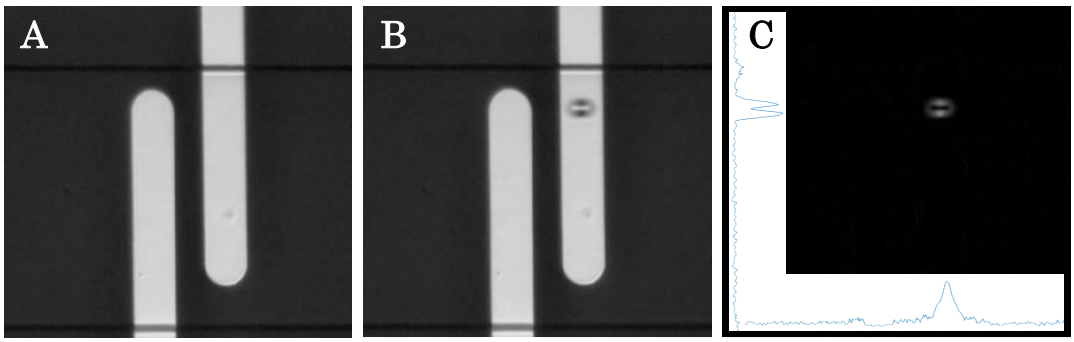

Figure 3.3: Algorithm steps of optical event detection. A) The reference frame, B) Event Frame, C) Matrice subtraction of the event frame from the reference frame.

In this measurement, one of the challenges we faced was the constant movement of the microparticles within the microchannel, resulting in less clear captured frames. To improve the resolution, we maintained a low flow rate, but even then, the resolution was not perfect. We attempted to implement autonomous circle-fitting algorithms to enhance the images, but they did not perform well due to shadowing issues. As a result, we resorted to a manual approach, wherein we measured the particle areas by drawing circles around the particle image five times and calculating the average number of pixels enclosed by the circle. Since we knew the pixel size from the microscope images, we were able to calculate the optical volume of the microparticles accurately.

Using this sensor design, we conducted measurements on three different analytes: 10 μm polystyrene, 20 μm polystyrene, and MDA-231 cells. Although

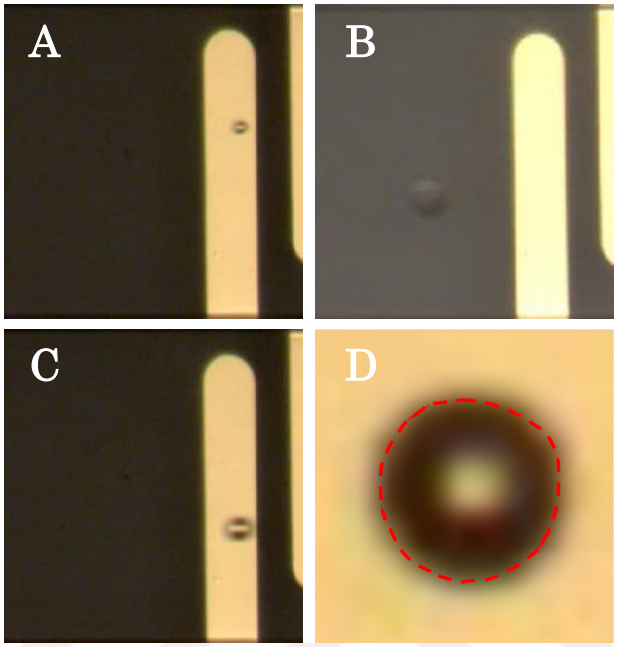

Figure 3.4: Event frames of different types of microparticles and area selection. A) 10 μm polystyrene, B) MDA-231 cells, C) 20 μm polystyrene, D) Example of area selection.

the results from the microwave measurements showed some scattering, the sensor's capability to differentiate between inorganic materials and organic cells was successfully demonstrated as expected. Notably, for microparticles of the same size, the signal from polystyrene particles appeared larger than that of cells. This difference can be attributed to the difference in dielectric permittivity between the materials and the surrounding media ($\epsilon_m = 78$). With a lower dielectric permittivity of polystyrene ($\epsilon_{pss} = 2.25$) compared to cells ($\epsilon_c = 40\text{-}60$), the Clausius-Mossotti factor for polystyrene resulted in a higher value, leading to a distinguishable response in the microwave measurements.

To enhance the throughput of the sensor, we made modifications by introducing a series of chevron-shaped electrodes. This alteration facilitated the use of dielectrophoresis (DEP) to focus the microparticles toward the center of the channel. Each set of consecutive electrodes with opposite potentials generated a DEP force, particularly effective in the focusing of larger microparticles. However,

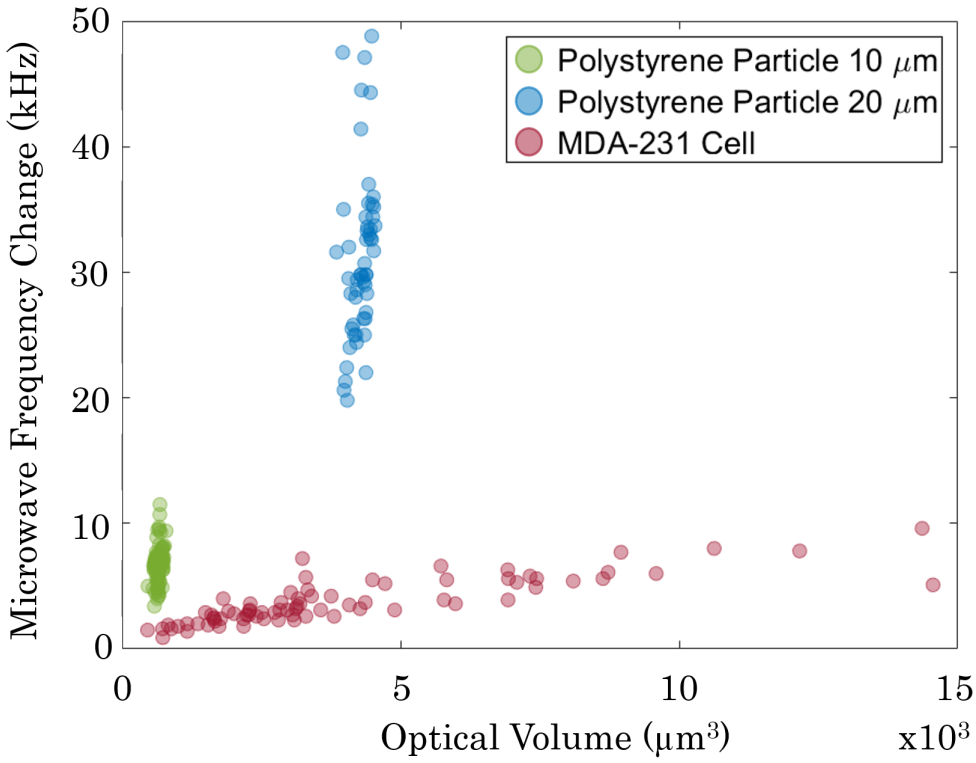

Figure 3.5: Experimental results obtained by the microwave sensor with optical imaging.

we observed that the focusing effect was less pronounced for smaller microparticles. Figure 3.6 illustrates the focusing effect observed in consecutive frames. For instance, a 20 μm particle was effectively focused within two-step periods, displaying a noticeable change in its position towards the center of the microchannel. On the other hand, a 10 μm particle experienced only a slight change as it passed through the center of the microchannel. This observation indicates that while the chevron-shaped electrodes demonstrated satisfactory performance in focusing larger microparticles, they were less effective for smaller ones.

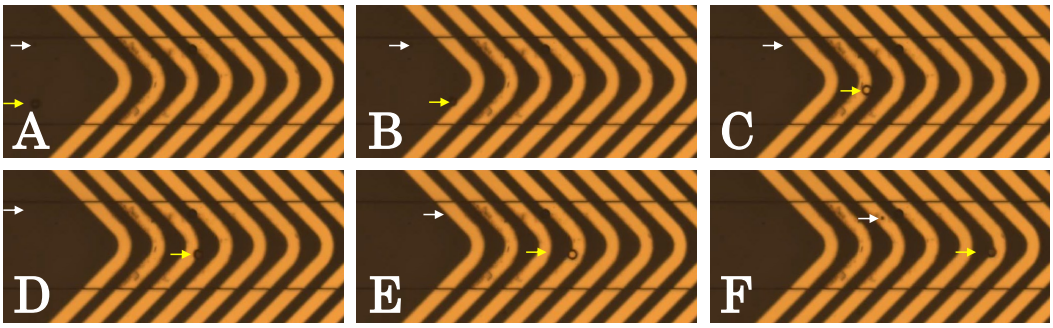

Figure 3.6: DEP focusing with chevron-shaped electrodes.

3.2 Microwave Sensor Combined with Impedance Cytometry

In this revised design, a large electrode pair was introduced, operating at the KHz-MHz frequency spectrum, and positioned to sandwich the microwave electrodes (as illustrated in Figure 3.7). The choice of fluid medium was altered to Phosphate Buffered Saline (PBS), a conductive solution facilitating current flow. The current within the designated frequency range led to the problem of double-layering on the electrodes exposed to the ionic medium. To mitigate its influence, emphasis was placed on maximizing the contact area with the medium while concurrently maintaining a minimal separation between the microwave electrodes to prevent any potential coupling between low and high-frequency signals.

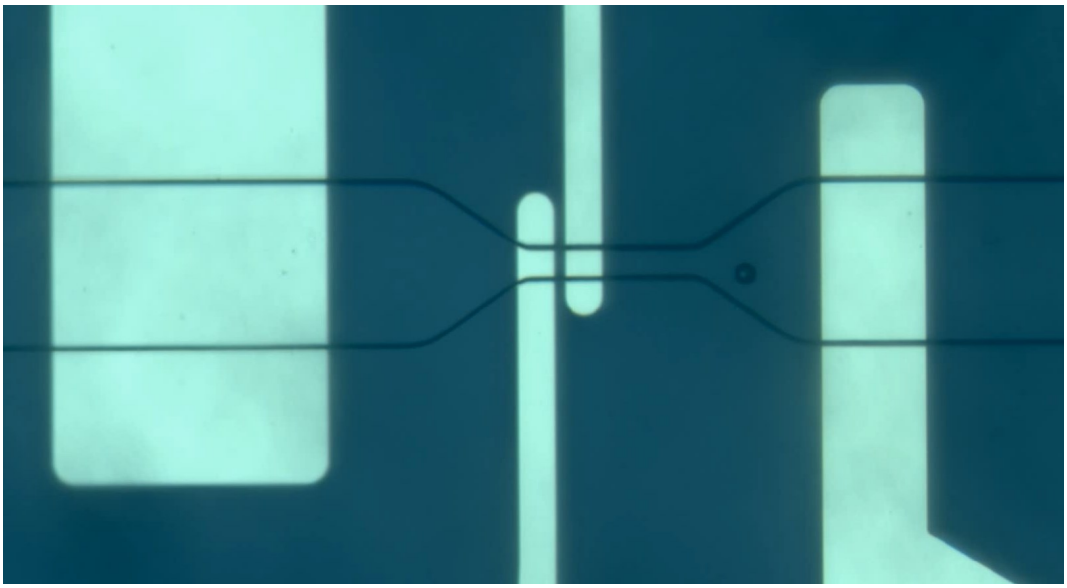

Figure 3.7: Sensing region of the microwave sensor combined with impedance cytometry. While the parallel microwave electrode pair is aligned with the microfluidic constriction, the impedance cytometry electrodes are placed on both sides to form a current flow.

A further modification included the introduction of a constricted segment within the microfluidic channel. Although the microfluidic placement step of the fabrication has become more challenging in this design, after some practice,

I was able to position the PDMS block with a few micrometers of precision. The implementation of the constriction guided all microparticles through a laterally uniform electric field formed between the microwave electrodes. Additionally, the impedance effect, which is proportional to the ratio of microparticle cross-sectional area to the microchannels, was enhanced. This adjustment resulted in an amplification of the low-frequency signal, boosting the geometrical size measurement sensitivity.

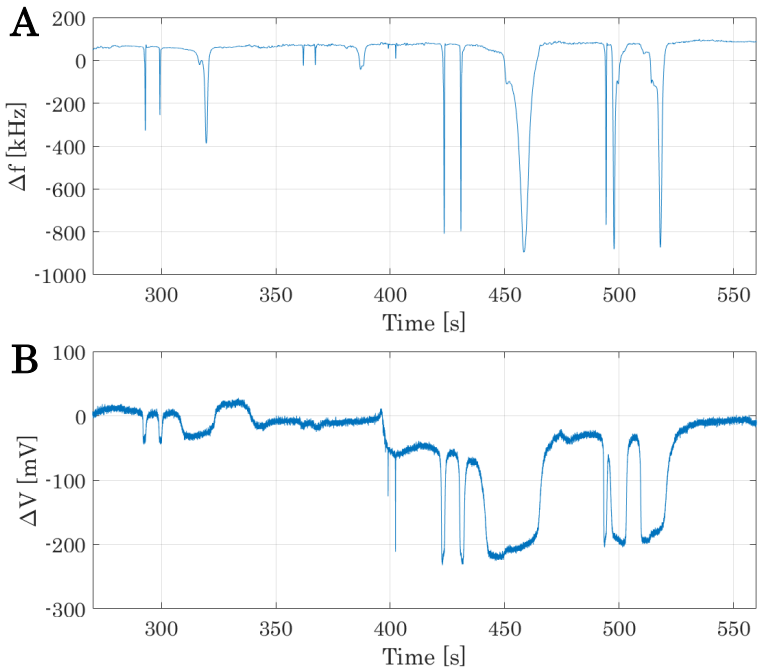

Figure 3.8: Baseline removed data of A) Microwave, B) Impedance cytometry on the first measurement. No significant drift is observed, therefore the sensor readings are consistent with each other.

Initially, the microwave frequency measurement technique mirrored the previous design. It employed a phase-locked control loop to trace the resonance frequency, allowing for the assessment of microparticle passage effects by monitoring frequency shifts (Figure 3.8A). To facilitate geometric volume calculations, the current signal was transformed into a voltage signal using a transimpedance amplifier. This voltage signal was subsequently processed with a lock-in amplifier for easy interpretation (Figure 3.8B). The impedance cytometry signal, depicted in the same figure, displayed peaks with widths directly correlated to the duration

a particle spent within the constricted microfluidic segment.

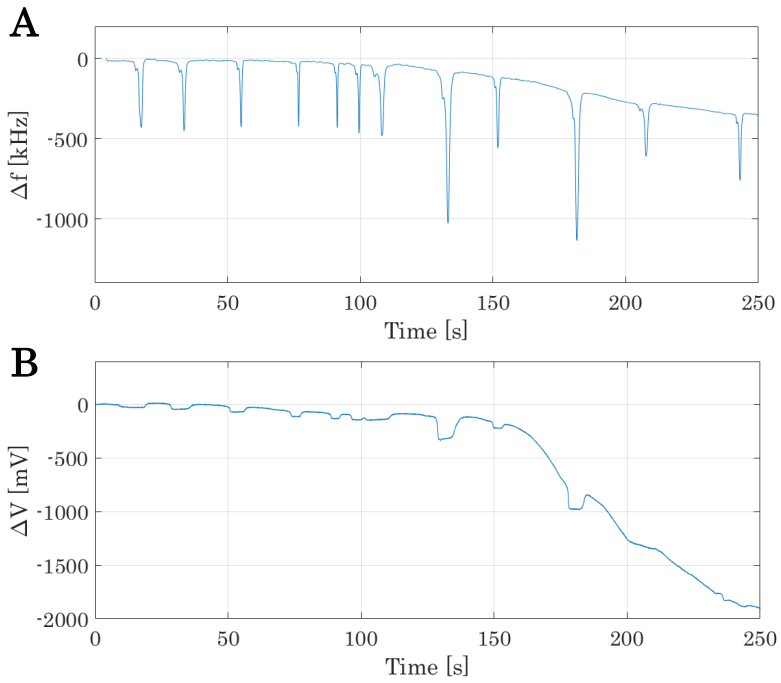

Figure 3.9: Baseline removed data of A) Microwave, B) Impedance cytometry on the second measurement. There is a significant drift in the sensor readings, therefore the event magnitudes are not as consistent as the first measurement.

Despite the sufficiently high signal-to-noise ratios observed in both high and low-frequency signals, the utilization of PBS, while not an ideal homogenous solution, introduced alterations to the resonance characteristics during the experiment. The inherent fluctuation in ion concentration within the PBS solution led to variations in the medium's conductivity, thereby causing different sensor readings even when dealing with identical particles. An illustrative instance of an obvious drift within the experiment is presented in Figure 3.9. Regarding the signal's interpretation of geometrical volume information, it relies on discerning the ratio of current flow and obstruction. To correct the signal, a reasonable approach involves normalizing the signal magnitude against its baseline. However, due to the nature of resonance, this strategy proved inadequate for mitigating a significant source of error in microwave measurements.

As the result of these two measurements conducted with 10 and 20 μm

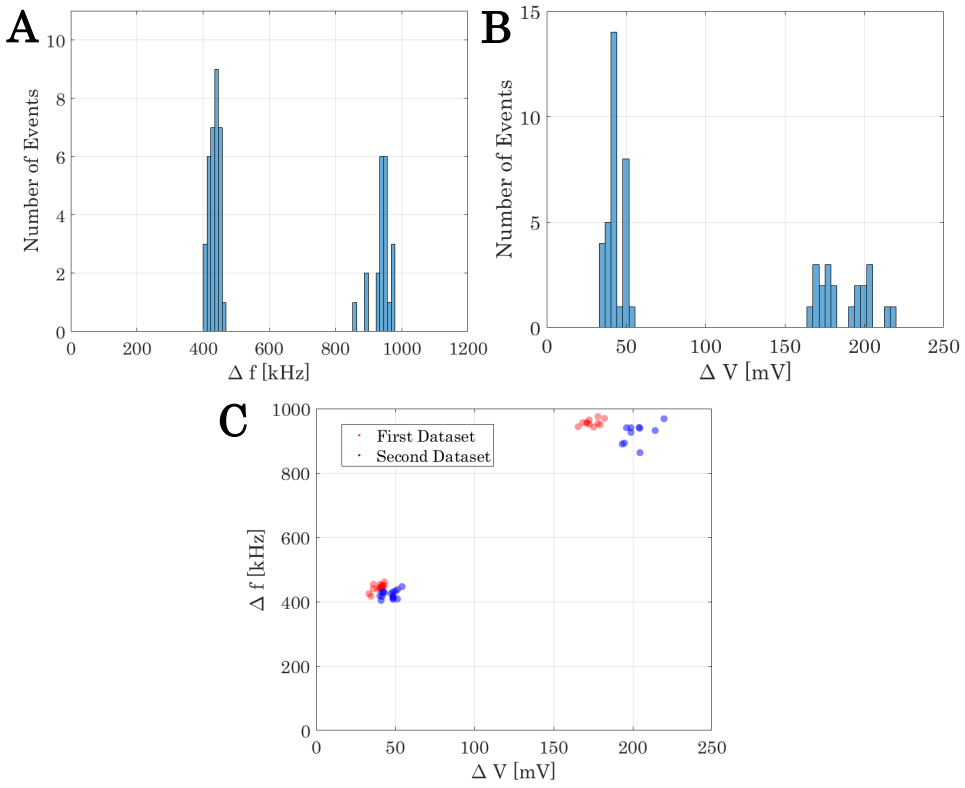

Figure 3.10: A,B) The microwave and impedance cytometry measurements of 10 and 20 μm polystyrene particles with phase-locked loop controller. C) Scatter plot of the signals

polystyrene particles, two concentrated accumulations occurred on both of the parameters. With the current closed-loop circuitry, it seems that while the microwave signal is proportional to the particle diameter, the impedance cytometry signal is proportional to the volume of the particle (Figure 3.10). However, the number of events were not sufficient to prove such relation and it was not feasible to increase the flow rate to increase the throughput of the device because the microwave frequency closed-loop controller was not fast enough to react shorter event duration. Therefore, we had to switch the microwave circuitry to be open drive (The details about the circuitry will be explained in the following section).

In this case, resonance tracking is not possible, however, the phase and amplitude of the microwave signals can be used to estimate whether the resonance

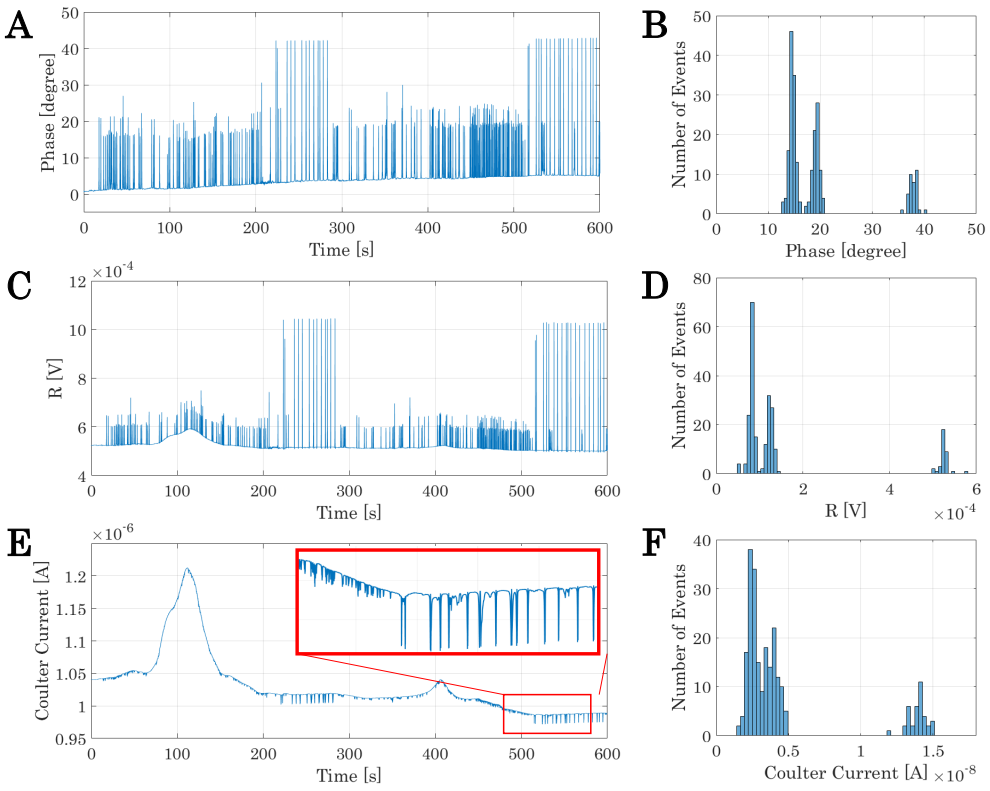

Figure 3.11: The microwave and impedance cytometry measurements of 10, 12 and 20 μm polystyrene particles with a consistent resonance characteristic by using an open drive.

characteristics are preserved or changed. On the other hand, the throughput increased significantly. In a 10-minute time period, we were able to measure more than 250 events which is a mixture of 10, 12 and 20 μm polystyrene particles. Three different parameters were obtained for each of them; microwave signal amplitude, microwave signal phase and impedance cytometry current as can be seen in Figure 3.11. The drift on the signals was quite tolerable in this experiment. The S11 open sweep measurements around the resonance frequency taken before and after the experiment matched nicely too.

With the open drive measurement, even 10 and 12 μm particles were distinguishable from each other with the microwave aspect of the sensor. The drift in the low-frequency signal was more drastic, therefore the differentiation was not as clear as it is in the microwave signals.

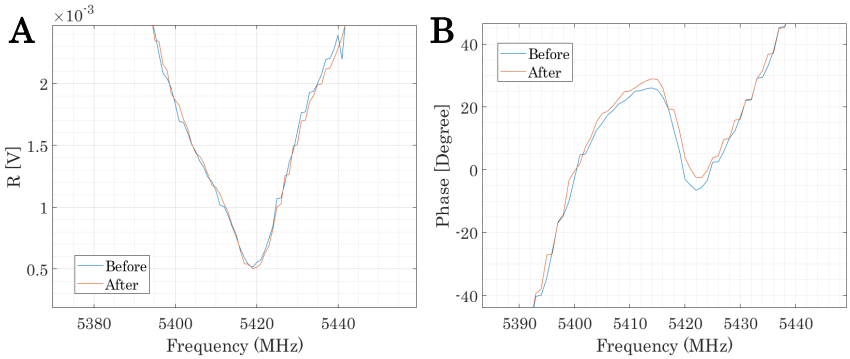

Figure 3.12: Frequency sweep of the S11 parameter before and after the experiment.

However, the physical representation of the amplitude (R) and Phase ($\Delta\theta$) were still unknown. Their relation with the particle size was different as can be seen in Figure 3.13. It seemed that the phase signal was proportional to the 1.5 order of the particle diameter while the amplitude signal was proportional to the volume. This contradiction raised the need for a repetition of the experiment.

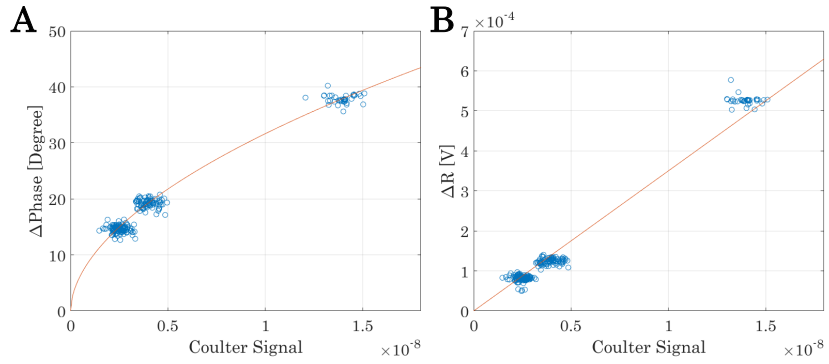

Figure 3.13: The relation between the low-frequency signal and microwave parameters.

The outcomes of the second experiment revealed remarkable findings. While the data was not feasible for distinguishing between various microparticles, the trend in the phase signal offered a crucial understanding of the microwave aspect of the sensor. From the open sweep, the resonance frequency was estimated to be 5410 MHz and the measurement was initiated with open drive mode. As the experiment progressed, significant alterations occurred in the resonance characteristics, causing the resonance frequency to increase by approximately 2 MHz,

as depicted in Figure 3.14C-D.

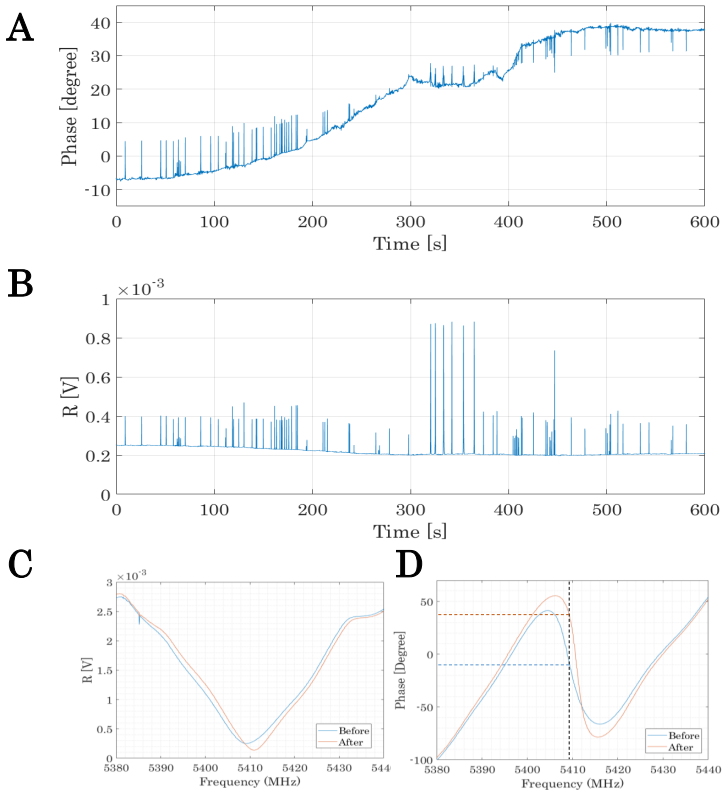

Figure 3.14: A,B) The phase and amplitude signals of 10, 12 and 20 μm polystyrene particles with varying resonance characteristics while using an open drive. C, D) Frequency sweep of the S11 parameter before and after the experiment. The difference

A particularly intriguing observation was that particle passages initially yielded upward spikes. Around the 5-minute mark, the phase parameter ceased to be responsive, prompting particle passages to progressively exert a downward effect on the phase signal. This sequence resulted in an overall shift of approximately 50 degrees in the phase baseline, which matches well with the open sweep measurement. Notably, the deviation in the open sweep phase value at 5410 MHz, before and after the experiment, correlated precisely with the observed baseline shift.

In contrast, the amplitude signal consistently displayed a unidirectional trend throughout the experiment, marked by only a minor downward inclination in the

baseline. From this experimentation, the insight emerged that the alteration in induced capacitance, caused by particles interacting with the sensor, could not be calculated using solely either the phase or amplitude of the signal. Instead, it appeared to be a combined function of the two.

3.3 Microwave Sensor Combined with Five Electrode Impedance Cytometry

In this revised design, measurements take place at different locations for both the low-frequency and microwave electrodes. As illustrated in Figure 3.15, the left side is equipped with five electrodes dedicated to low-frequency measurements, while the right side has two microwave electrodes.

To match the signals generated by a particle on both sensors, adjustments were made by placing the electrodes in closer proximity to the constricted section of the microfluidic channel. This alteration facilitated the synchronization of the low and high-frequency signals. However, the close placement of the electrodes introduced a coupling effect. Consequently, as a particle passes through the impedance cytometry electrodes, the microwave signal is also influenced. This effect adds complexity to data analysis and results in a reduction of the signal amplitude consequently diminishing the signal-to-noise ratio.

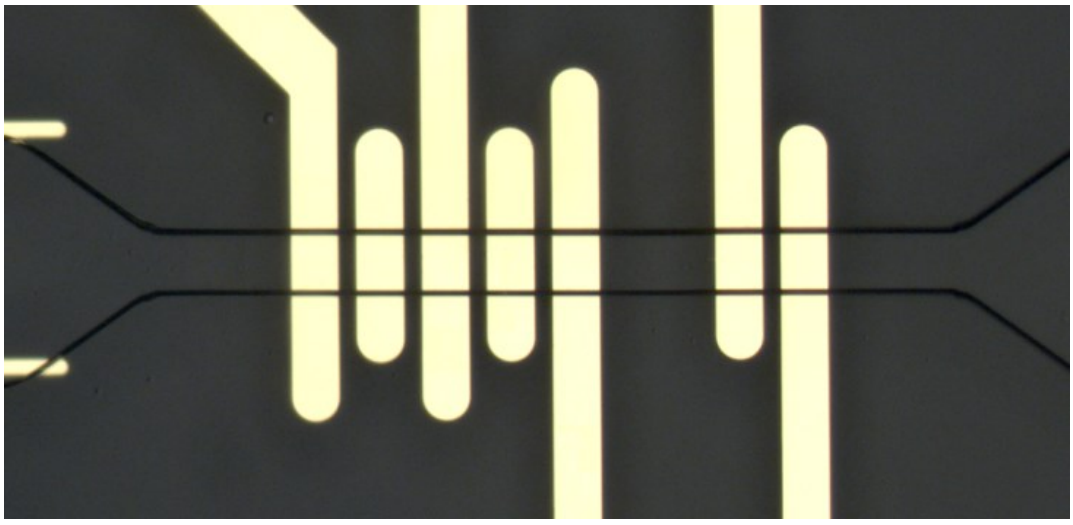

Figure 3.15: A micrograph of the sensing region.

The low-frequency part of the sensor closely follows the recent work [4, 33, 34, 29]. Here, a five-electrode arrangement was used to obtain the geometric size of the particles while calibrating for the effect of the height variation of

particles as they flow through the channel (Figure 3.15). In the five-electrode arrangement, the 3rd electrode is used to provide a 1 MHz AC excitation voltage while the 1st and 5th electrodes are used to collect the resulting differential current. This current is carried by the ions in the solution, and a non-conducting particle passing through the channel blocks the ionic motion, resulting in a drop in the current proportional to the particle's volume.

The remaining two electrodes, electrodes 2 and 4, were kept floating: they were used to facilitate the height measurements by modifying the current flow between the middle and outer electrodes. A particle passing near the bottom of the channel induces a large variation in the current along its trajectory, whereas the current waveform is smoother for an identical particle passing near the top of the channel. This way, the variation in the current for each trajectory was encoded by the ratio between the large and small peaks in the signal waveform (Figure 3.16B). This ratio, prominence (P), was then used to calculate the height of each particle and calibrate its response to obtain the geometric size accurately.

For the size and height measurement by the low-frequency sensor, the 3rd electrode is driven by a 1 V peak-to-peak signal at 1 MHz and the resulting current is collected from the outer electrodes by a differential readout configuration. The current signals were converted into voltage by a transimpedance amplifier (Zurich Instruments, HF2TA), and read out by a lock-in amplifier (Zurich Instruments, HF2LI) in differential mode.

For the electrical volume measurements at microwave frequencies, after verifying the resonance characteristics of the SRR with a vector network analyzer (VNA), we switched to our custom circuitry (Figure 3.16A) and set the frequency of the signal generator to the resonance frequency (5.4 GHz). The circuit consists of two lock-in amplifiers to employ single-sideband modulation (SSBM) and a signal generator as signal sources. We fed the SRR at its resonance frequency with 500 mVpk power output. The time constant of the lock-in amplifiers was set to 501 μs and the sampling rate was 13.39k/sec to fully detect rapidly passing particles. Since the maximum operational frequency of the lock-in amplifiers was

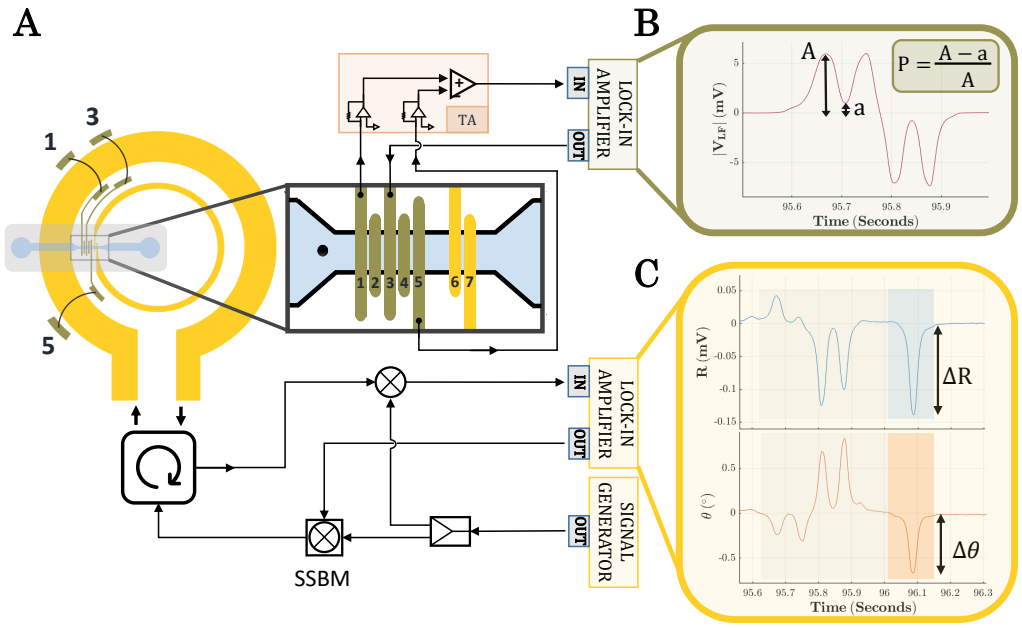

Figure 3.16: A) Schematic of the circuit, SSBM: single side-band modulator, TA: Transimpedance Analyzer. B) Low-frequency current signal of a passing particle forms a bipolar Gaussian shape. The geometric size and height values of the particles are calculated from this measurement. C) Microwave signals induced by a passing particle. The change in amplitude (R) and phase (θ) values in the highlighted sections are used to calculate the capacitance change induced by the particle.

below the resonance frequency, we built a custom Single Side Band (SSB) heterodyne circuitry [20, 19]. The reference signal outputs of the lock-in amplifiers were up-converted before entering the resonator and down-converted before digitally reading the amplitude and phase of the signal.

With this design, we also solved the relation between the induced capacitance caused by the particles and the microwave parameters; amplitude, and phase. The sensor's microwave part is modeled as a resonating RLC circuit and the out-of-phase component which is explained in the 2.1.3 section is calculated. With this method, any fractional change in the capacitance of the microwave resonator is reflected in the out-of-phase component as in Equation 2.9

With this technique, we compared the measurements of two types of microparticles, polystyrene and soda-lime glass. Polystyrene microparticles had a fixed diameter value of 20 $\pm$ 0.3 μm while soda-lime glass particles were reported to have diameters changing in the range of 15-22 μm. Therefore, it is expected that soda-lime glass particles will have a much wider size distribution.

The electrical diameter is the square root of the derivative of the out-of-phase component and the geometrical diameter is the cube root of the change in the impedance cytometry signal.

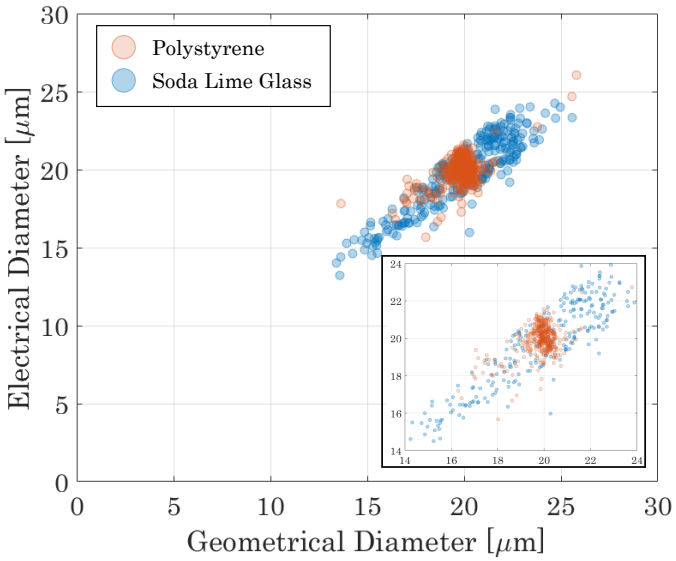

Figure 3.17: Separation of polystyrene and soda lime glass using geometric and electrical diameters.

$$\frac{\text{Electrical Diameter}}{\text{Geometric Diameter}} = \frac{\sqrt{\Delta Y}}{G\sqrt[3]{A}} \approx \sqrt{K_{CM}} \tag{3.1}$$

These values are multiplied with constants G1 and G2 to have a mean of 20 μm for polystyrene particles. Soda-lime glass particles are calibrated accordingly. The ratio of these two materials' slope on the geometrical versus electrical diameter figure was thought to be proportional to the $|K_{CM}|$ value for each particle (polystyrene and soda-lime glass are 0.48 and 0.43, respectively). Even though

the geometrical size range was correct according to the manufacturer's (Sigma-Aldrich,74491-10ML-F, Cospheric, SLGMS-2.5) specifications and the slope of the polystyrene (1.02) was a little bit larger than soda-lime glass (0.99), due to lack of the signal to noise ratio the differentiation was not adequate as can be seen from Figure 3.17.

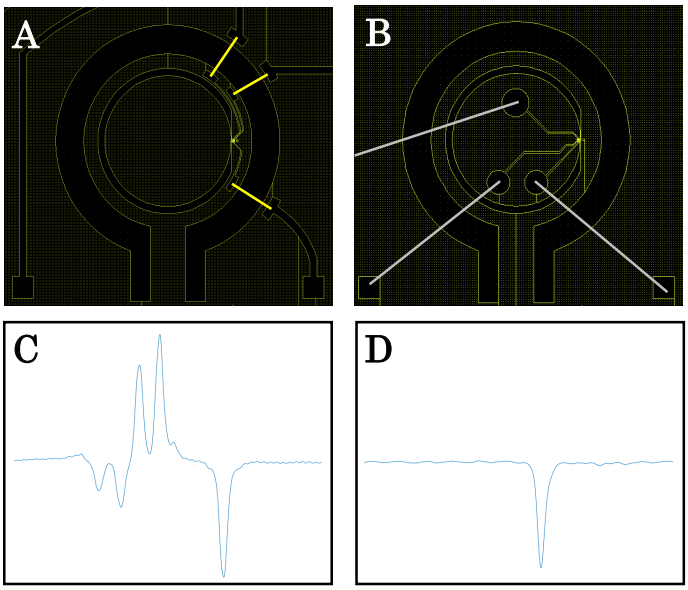

Figure 3.18: A) Layout Editor drawing of the initial design with wire bonds indicated as yellow lines. B) Layout Editor drawing of the modified design with the soldered wires indicated as gray lines. C) Effect of a particle passage on the phase signal for the initial design. The coupling effect of low and high-frequency electrodes is very strong. D) Effect of the particle passage on the phase signal for the modified design. The coupling effect is prevented. The signal shape is easier to detect and analyze.

Following this experiment, the sensor design underwent an iteration with the objective of minimizing coupling effects and enhancing the signal-to-noise ratio. To achieve this aim, a revision was made to the layout: the gold pads of the low-frequency electrodes were relocated to the inner ring rather than being positioned between the inner and outer rings. Moreover, the method of establishing electrical connections was modified: soldering thicker wire (depicted as gray lines in Figure 3.18B) was employed instead of thin wire bonds (as seen in Figure 3.18A, represented by yellow lines) to enable the transmission of the low-frequency current to the impedance cytometry electrodes. As a result of these adjustments,

the phase change occurring as a particle traverses the sensing region transitioned into a simple, singular peak (as illustrated in Figure 3.18D). This differed from the more complex shape (depicted in Figure 3.18C) observed in the initial design.

Later on, the microparticle material classification experiment was repeated using the modified design. The increased signal-to-noise ratio yielded a significantly better differentiation as can be seen in Figure 3.19A. Specifically, polystyrene particles exhibited a concentrated distribution of around 20 μm, while soda-lime glass particles were scattered within the 15 to 22 μm range. Unlike the previous experiment, the particles were introduced to the sensor within a single solution this time. Consequently, evaluating the accuracy of differentiation was not feasible. However, by drawing a separation line between the clusters, a large portion of the particles appears to have been successfully differentiated. Figure 3.19B presents a histogram displaying the ratio of electrical to geometrical diameter, with a separation line corresponding to the one shown in Figure 3.19A. Distinct accumulations emerged for different types of microparticles.

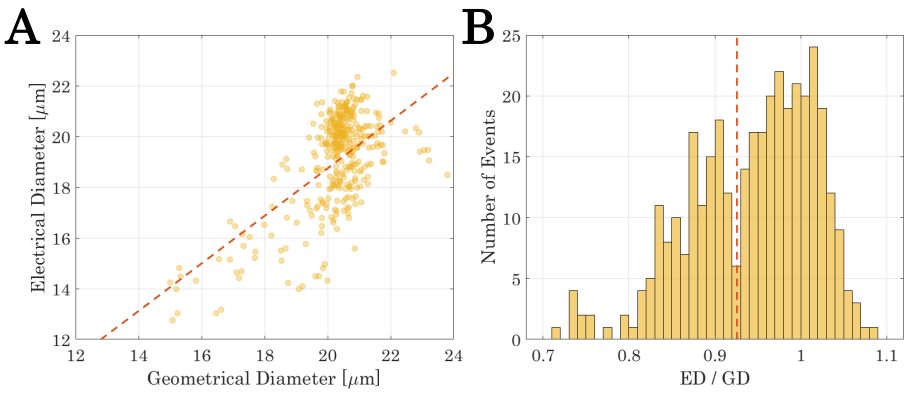

Figure 3.19: A) Geometrical versus electrical diameter distribution of a mixed solution of polystyrene and soda-lime glass microparticles B) Histogram showing the distribution of the ratio of electrical to geometrical diameter

3.4 Microwave Sensor with Varying Electrode Gap Size

Apart from previous designs aimed at classification or geometrical size measurements, we also worked with designs that aim to explore adaptable features through different electrode geometries. In this specific configuration depicted in Figure 3.20, by making a double measurement for each particle, we aimed to infer their position in the microchannel while they are passing through the sensing region. This design features three microwave electrodes. Notably, the left and right electrodes are connected, effectively sharing the same potential. To simplify explanations, these two electrodes will be referred to as the 'Ground' electrodes, while the middle one will be termed the 'Signal' electrode within this chapter.

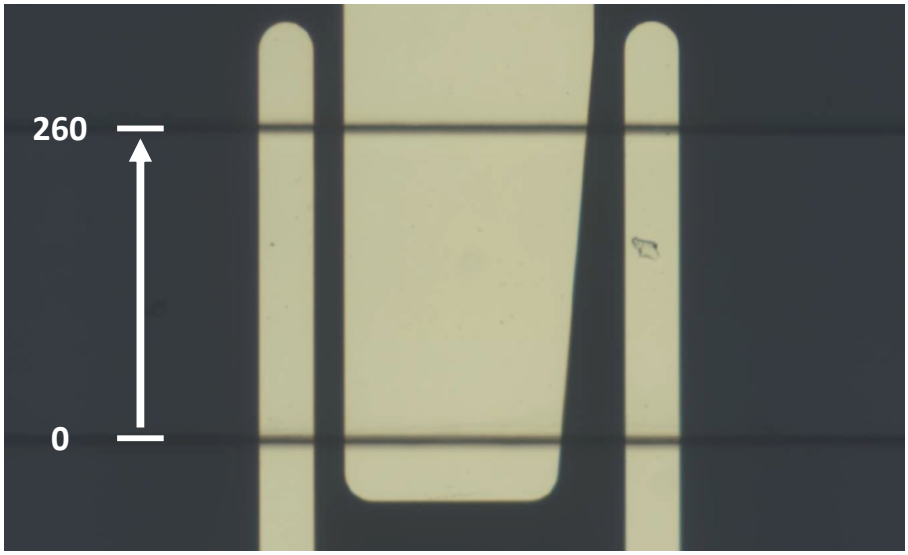

Figure 3.20: Sensing region of the microwave sensor with varying electrode gap size

Unlike conventional electrode pairs, the alignment of the signal electrode on the right side isn't parallel to the ground electrodes. Consequently, the electric field generated between this electrode pair lacks uniformity in both the vertical and lateral directions due to the varying distance between them. We used this uniformity to determine its position by comparing it with the signal from the

parallel electrode pair.

For the left parallel electrode pair, the magnitude of the microwave signal is determined by three factors: particle material, size, and vertical position. On the right side, the lateral position of the particle also exerts an influence. This experiment focuses solely on 20 μm polystyrene particles, effectively eliminating dependencies on material and size. Additionally, due to the limited likelihood of significant vertical position changes between gaps, we consider the vertical position to remain constant for both measurements. Consequently, the only parameter affecting the ratio of signal magnitudes is the lateral position.

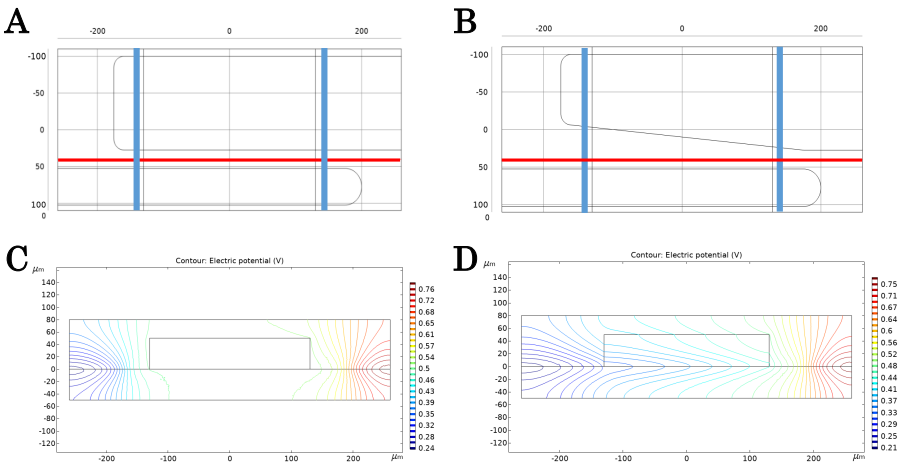

Figure 3.21: A) Sensing region of the parallel electrode pair. The blue lines denote the microchannel walls. The red line corresponds to the cross-section, indicated in part C, positioned at the midpoint of the gap. B) Sensing region of the inclined electrode pair. The blue lines represent the microchannel walls. The red line corresponds to the cross-section taken for part D. C) Electric potential distribution across the parallel electrode pair. The electric potential maintains uniformity within the microchannel. D) Electric potential distribution across the inclined electrode pair. The electric potential increases on the right side and gradually decreases towards the left side.

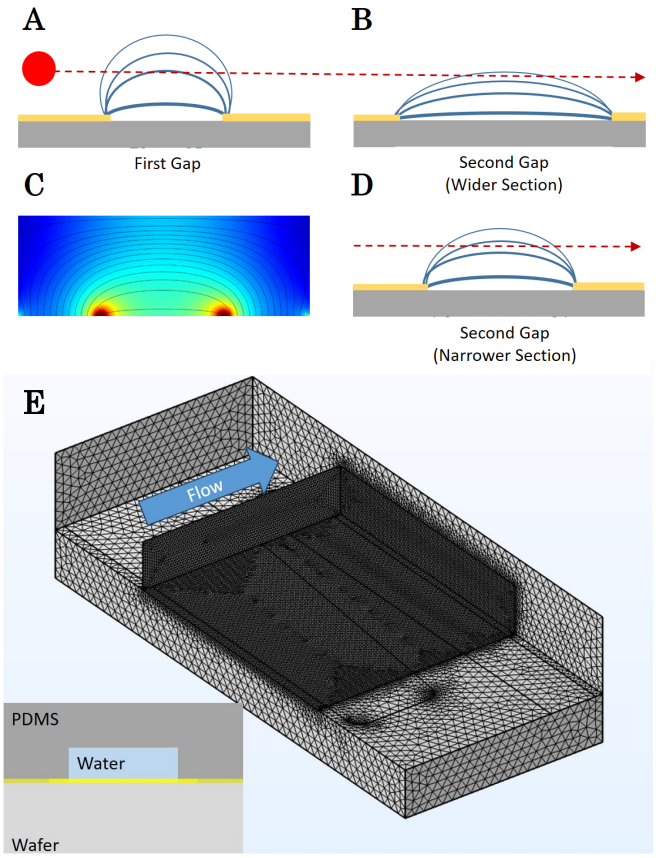

Figure 3.22: A) Schematic representation of the electric field for the parallel electrode pair. B) Schematic representation of the electric field within the wider section of the inclined electrode pair. C) Cross-sectional view extracted from the COMSOL simulation showing the electric field dynamics of the parallel electrode pair. The black lines indicate the electric field lines, while the color map illustrates the electric field magnitude. D) Schematic representation of the electric field within the narrower section of the inclined electrode pair. E) Mesh distribution displayed in the COMSOL simulation. Notably, due to the microfluidic region's significance, a finer mesh is employed within this domain.

Based on the Comsol Multiphysics simulation screenshot in Figure 3.22C, the formation of electrical field lines is represented by the black curves, while the distribution of electric field magnitude follows the color indications (with red signifying high and blue signifying low values). Figures 3.22A, 3.22B, and 3.22D show the influence of gap distance on electric field lines schematically. In the initial gap, which maintains a consistent 24 μm dimension, the electric field between the enclosing electrodes remains constant by lateral positioning. Contrastingly,

the electric field associated with the second gap diminishes from 55 to 30 μm as the gap distance increases relative to the lateral position. A red trajectory line connecting Figures 3.22A and 3.22B serves as a representation of the influence of height on the electric field. For equivalent heights, the first gap forms a stronger electric field than the second gap, implying that the microwave signal ratio for the 2nd Gap / 1st Gap is consistently less than one and reveals lateral position information.

Later on, a trial involving 30 μm diameter polystyrene particles was conducted to evaluate the design concept. To validate the lateral position of the particles, the microscope camera recorded the sensing region, employing the same methodology as in Chapter 4.1. As anticipated, the signal ratios acquired from the gaps were consistently below one, exhibiting a trend line aligned with the microchannel's lateral position (as indicated by the blue dots in Figure 3.24). However, the trend line's distribution was more scattered than anticipated, with signal ratio variations extending up to 0.15 for the same lateral position. This situation raises the question of whether there might be another factor influencing signal amplitude or ratio. The initial hypothesis suggested the possibility of height variation playing a role.

In order to understand the impact of particle height on signal amplitude, further simulations were conducted. The microchannel measured 260 μm in width and 50 μm in height. Given the utilization of 30 μm particles, their center could occupy a lateral range of 16 to 244 μm and a vertical range of 16 to 34 μm and in total 12 microparticles are placed in these extreme positions and centers for both of the gaps as can be seen in Figure 3.23. To prevent mesh-related errors, all the particle geometries are built in each run, and only one of the materials is assigned to be polystyrene. Others were defined as PBS.

Simulating the entire resonator system and attaining a satisfactory mesh quality in the sensing region demanded an immense computational workload. Consequently, we opted to limit the simulation scope to the sensing region, including the base (Fused silica wafer) and the top volume (PDMS) as the simulation space. In COMSOL, the AC/DC / Electric Fields and Currents / Electric Currents branch

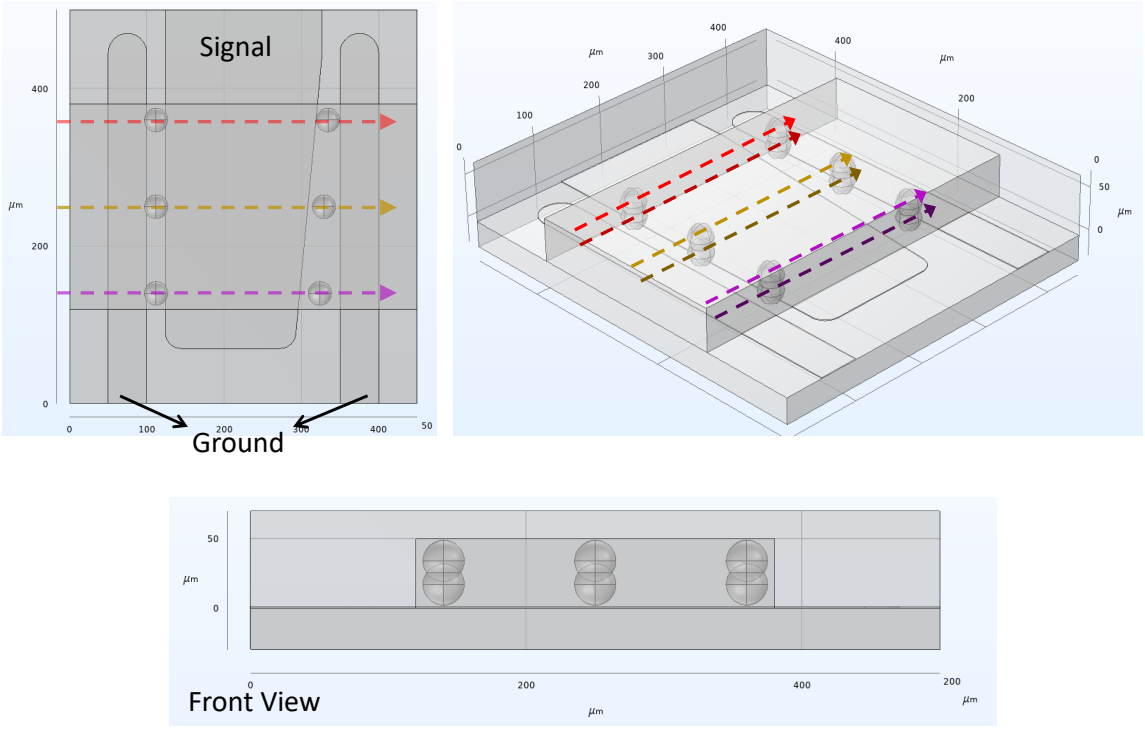

Figure 3.23: COMSOL simulation geometry.

within the physics tree was selected, employing a frequency domain study. The middle electrode was assigned as a Terminal with a potential of 1V, while the outer electrodes were set as ground. Material properties were assigned with values at 5.4 GHz, and the simulation was executed. In COMSOL, there isn't a direct option to compute the capacitance between a terminal and ground. However, it can compute the admittance (Y), which comprises two terms:

$$Y(\omega) = G + j\omega C \tag{3.2}$$

Here, G represents conductance, and C stands for capacitance. Given that the conductance value is approximately 10^{-17} and the capacitance value is on the scale of 10^{-14}, the dominant factor in admittance is the capacitance value. Thus, by dividing the admittance by $j\omega$, we can effectively derive a robust estimate of the capacitance within the sensing region.

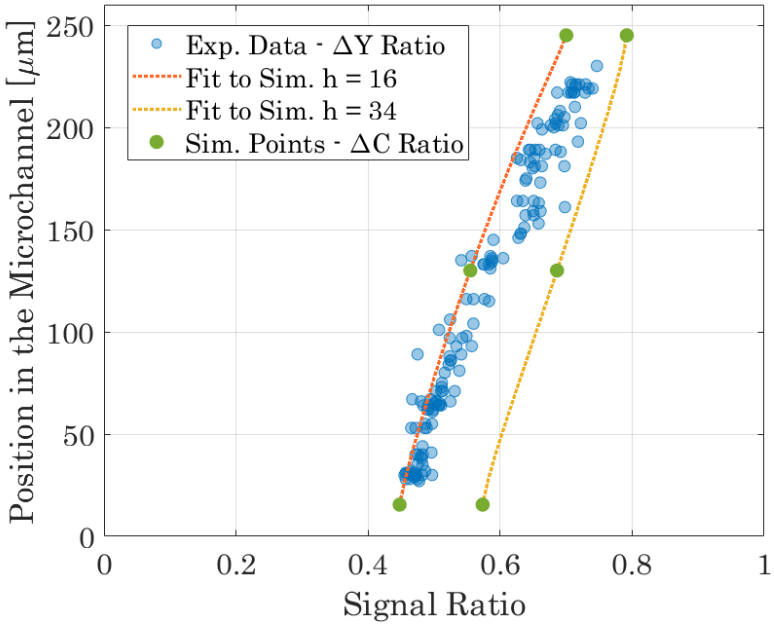

Figure 3.24: Relationship between signal ratios and the lateral position of particles, depicted through correlation analysis. Experimental results are represented by blue dots, while simulation outcomes are shown by green dots. Dotted curves correspond to interpolated curves connecting simulation points.

The capacitance values for both the empty channel (Only PBS) and with particles in distinct positions are calculated. Later on, the signal ratios for identical lateral and vertical positions in each sensing gap are computed. The correlation between these ratios is visually depicted in Figure 3.24. The experimental results align closely with the range of simulation outcomes. As particles approach the lower surface of the microchannel, the signal ratio diminishes, and conversely, it increases as they move away. This implies that if the precise lateral position of a particle can be determined via camera observation, it becomes possible to deduce the particle's vertical position as well. While the practical application of this technique might be limited, it served as an inspiration for the development of the ultimate generation sensor design.

3.5 Microwave Sensor with Different Gap Size Electrode Pairs Combined with Impedance Cytometry

This iteration represents the most recent sensor design advancement, combining previous iterations' finest attributes and introducing further enhancements. Similar to the designs in Chapters 4.2 and 4.3, a low-frequency signal is used to measure the geometric volume and a high-frequency signal is used to measure the electrical volume of the particles to calculate their Clausius Mossotti factor and subsequently dielectric permittivity. The experimental results of this design will be explained in the following chapter.

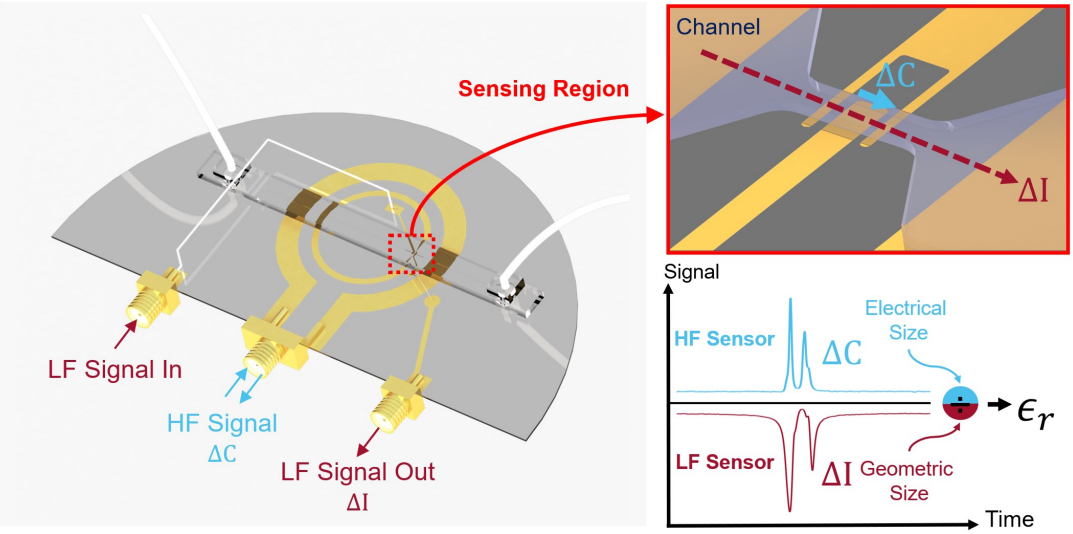

Figure 3.25: Sensor configuration

It uses the same impedance cytometry electrode shape detailed in Chapter 4.2 with a shorter constriction region which theoretically enables a throughput potential of up to 500 events per second, with a measurement duration of 20 milliseconds per event. In this design there are no coupling effects between low and high-frequency signals, thereby yielding the highest signal-to-noise ratio among all prior designs. For instance, while measuring a 20 μm polystyrene particle, the signal-to-noise ratio of 1400 for phase, 800 for amplitude, and 400

for impedance cytometry measurements is achieved. Remarkably, these measurement quality levels surpass those of the state-of-the-art microwave sensors currently available [21]. For compensating height variations, a microwave sensing region featuring two distinct gap sizes is implemented. This technique draws inspiration from the correlation between height and the electric field in the microwave sensor with variable electrode gap sizes. Within this design, different electric field magnitudes varying with height are formed by employing two microwave gaps with dimensions of 15 and 25 μm. Through this geometry, two distinct height compensation methods are integrated into the microwave aspect of the sensor. The first method relies on the ratio of microwave signals measured in each gap, while the second method leverages particle velocity for compensation.

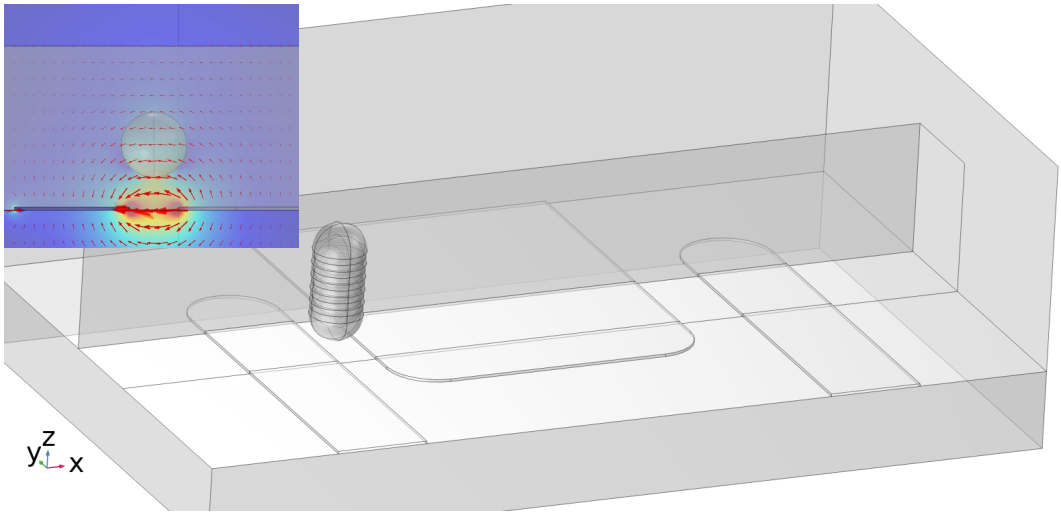

Figure 3.26: COMSOL Simulation geometry for different vertical position particles.

The primary rationale for incorporating two gaps of varying sizes was to employ the first height compensation approach. The second method was discovered subsequent to experimentation. Prior to the experimental phase, a series of COMSOL simulations were conducted with the geometry depicted in Figure 3.26.

The initial simulation validates the impact of the vertical position of the particle on capacitance change. To explore this, three particles of distinct sizes (15, 20 and 25 μm) are positioned within the first gap at five different height levels (15, 20, 25, 30, and 35 μm). As illustrated in Figure 3.27A, the diminishing effect

of height on particles remains consistent across various particle sizes. As a note, since the dielectric permittivity of polystyrene (2.5) is smaller than water (78), the capacitance change has a negative value.

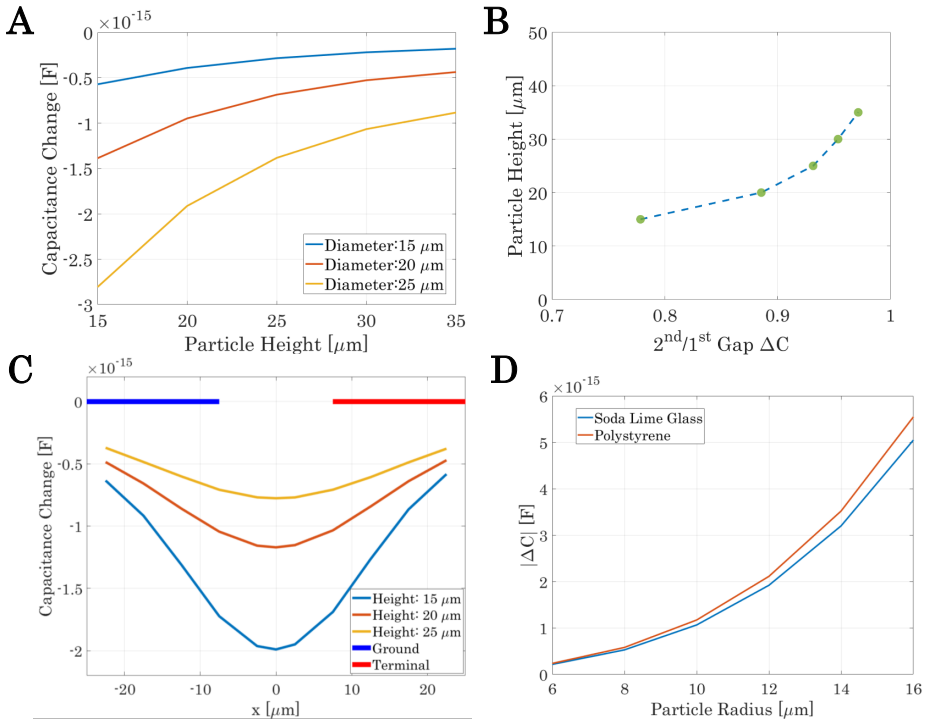

Figure 3.27: Results from COMSOL simulations are presented as follows: A) Relationship between particle height and induced capacitance for various particle sizes. B) The ratio of induced capacitance when a particle passes through the gaps. C) The influence of the lateral position of the particle on the amount of induced capacitance. D) Induced capacitance measurements for polystyrene and soda-lime glass of different sizes.

Upon normalizing the signal to that of the 15 μm particle height, the attenuation coefficients were consistently 0.60, 0.41, 0.31 and 0.25 for all particle sizes. The identical simulation process is replicated for the wider gap, yielding consistent results but distinct from those of the first gap. The attenuation coefficients, which stand at 0.68, 0.49, 0.38, and 0.31 for all particle sizes, further underline this observation. This variation in the attenuation coefficients between the gaps for particles of the same height validates the suggested methodology. This distinction is also visually apparent in Figure 3.27B, where the ratios of capacitance change triggered by same-sized particles at varying vertical positions are

demonstrated. As anticipated, there is not a linear trend.

In the following series of simulations, we analyzed the most influential lateral positions of particles around the sensing gaps. A concern arose due to the difference in the electrode areas—ground electrodes being smaller than the terminal electrode. We were apprehensive that the surface charge density might result in uneven potentials along the closest edges of the electrodes, leading to an asymmetrical electric field concerning the gap's center. To assess this, we employed the same geometry. However, instead of placing the particles in the center of the sensing gaps, we gradually shifted them horizontally by 45 μm while computing the capacitance change each time. We conducted this procedure three times, each with varying vertical particle positions at 15, 20, and 25 μm.

As depicted in Figure 3.27C, for each height value, the most significant change in capacitance occurred when the particle was positioned in the middle of the sensing gap. Please note that the schematic representation of the ground and terminal electrodes in the figure (blue and red, respectively) is for illustrative purposes and does not represent any specific data.

In the final set of simulations, we aimed to illustrate the variations in induced capacitance among different material particles. We constructed particles of various sizes (6, 8, 10, 12, 14, and 16 μm) at the center of the narrower microwave gap. For each size, we assigned two different materials—polystyrene and soda-lime glass—and computed the resulting capacitance changes. In a medium of water at 25°C with a conductivity of 9 mS/cm, operating at 5.4 GHz, these materials exhibited Clausius-Mossotti factors of -0.47 and -0.43, respectively, with a ratio of 1.093. In accordance with the simulation results, the ratio of induced capacitance values remained constant at 1.099 for particles of constant radius. This finding reinforces the notion that with a sensor that has a signal-to-noise ratio higher than 100, material differentiation should indeed be feasible even for different-sized particles.

Once the design is validated through these simulations, the circuit implementation proceeds with the connections shown in Figures 3.28A and 3.29A. Similar to

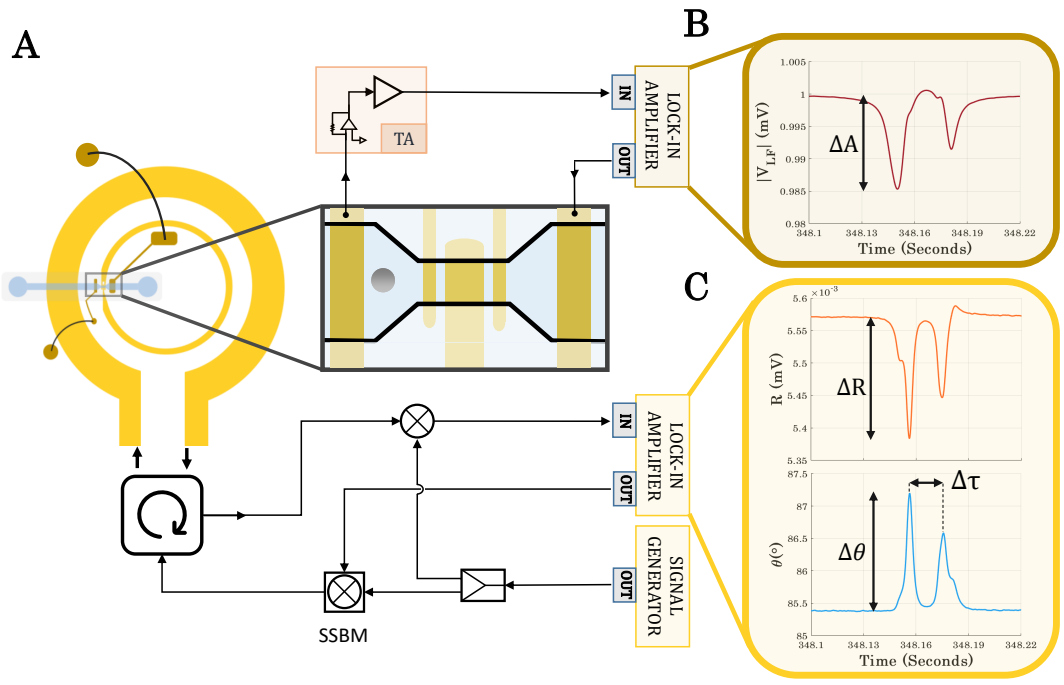

Figure 3.28: A) Schematic of the circuit. B) Normalized low-frequency signal of a passing particle. The initial dip conveys size-related information. C) Microwave signals induced by a passing particle. The initial dips of both the amplitude and phase signals convey the dielectric property information. The second peak is used for height calibration.

the configuration used in the microwave sensor combined with the five-electrode impedance cytometry design, we utilize two MFLI lock-in amplifiers to construct a single-sideband modulation and an HF2LI to facilitate impedance cytometry measurements alongside an HF2TA transimpedance amplifier. The low-frequency signal is transmitted out of the SRR region via wire bonds. A section of the raw data spanning an event duration is demonstrated in Figures 3.28B and 3.28C. To eliminate the influence of conductivity fluctuations on the current blockage magnitude, the impedance cytometry signal (V_{LF}) is normalized with respect to its baseline, resulting in voltage levels of approximately 1 mV.

One might wonder why there are two dips in the low-frequency signal, despite the existence of only one constriction along the microfluidic channel. This phenomenon can be attributed to electrode number 4 in Figure 3.29B. Typically,

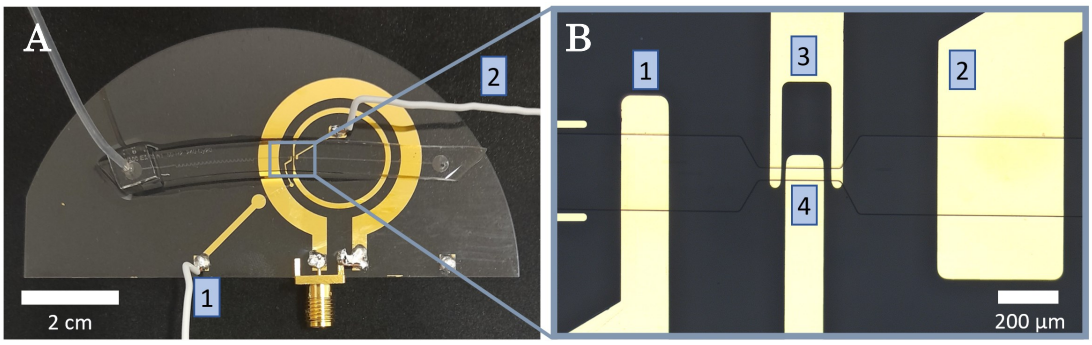

Figure 3.29: A) Photo of the sensor B) Micrograph of the sensing region

impedance cytometry current flows between electrodes 1 and 2 through the conductive PBS solution. However, in this design, the extensive gold surface of the 4th electrode covers a substantial portion of the microfluidic constriction. Given that gold has a significantly higher conductivity than the PBS solution, within the region where the 4th electrode coincides with the constricted area, the impedance cytometry current traverses through the gold layer on the channel's bottom rather than the solution. In this region, as the current bypasses the solution, dielectric particles are unable to obstruct its flow. Consequently, the presence of a particle on the 4th electrode has a neutral impact on the impedance cytometry signal.

The impact of a particle on the low-frequency signal begins as it approaches the entrance of the microfluidic constriction and gradually diminishes as it exits. The buffer region between the wider and constricted sections of the channel also influences the initial and final segments of the low-frequency signal, as evident in the first and last rows of Figure 3.30B. Conversely, the microwave signals exhibit significant responses only when a particle precisely aligns with the sensing gaps, as depicted in the third and fifth rows of Figure 3.30C and 3.30. The minor coupling effect between the microwave and low-frequency signals is observable as a slight bump in the second row of Figure 3.30C and the sixth row of Figure 3.30D. Nevertheless, it's worth noting that the signal-to-noise ratio is exceptionally high compared to previous designs.

Following the initial experimentation with 20 μm polystyrene particles, a correlation [33] appeared between the ratio of peaks in a microwave parameter and

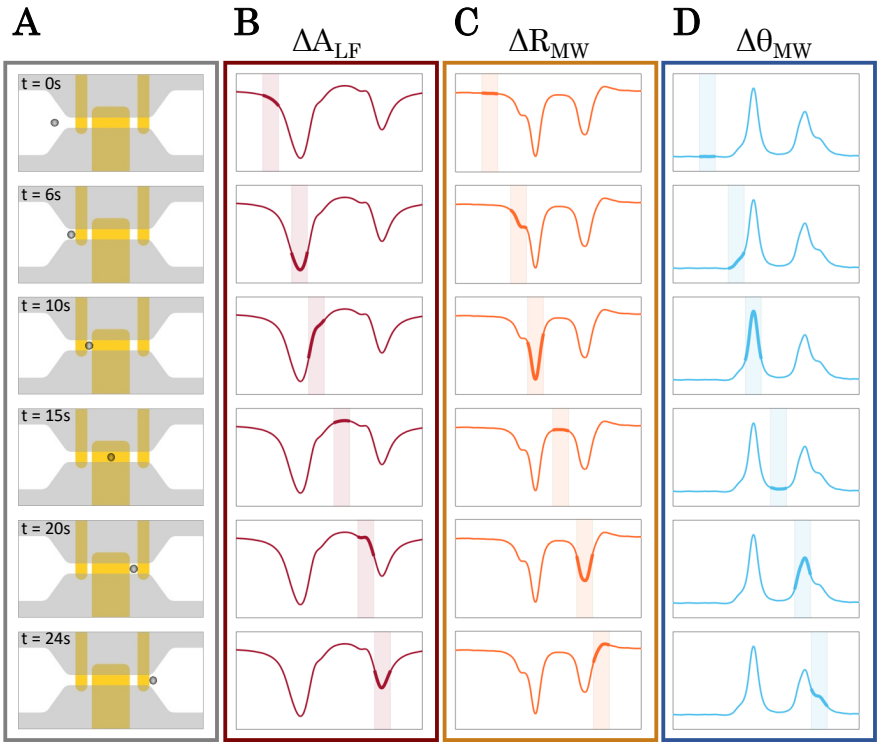

Figure 3.30: The impact of particle passage through the microfluidic constriction on sensor parameters. The highlighted sections of the signals correspond to the instants given in part A. A) Timing and particle position. B) Low-frequency signal. C) Amplitude and D) phase of the microwave signal.

particle velocity. It's observed that particles inducing higher ratio values move at faster velocities, suggesting their movement at higher positions within the channel. Conversely, those with lower ratios tend to occupy lower positions, as depicted in Figure 3.32A.

This observation is subsequently put to the test using the five-electrode configuration, which measures particle vertical position via a distinct method (Prominence calculation). The same trend occurred; faster particles tended to occupy higher vertical positions as can be seen in Figure 3.32B. The consistent correlation observed across both designs further solidified the height compensation method based on particle velocity.

The underlying principle of this phenomenon involves the parabolic velocity profile exhibited by fluid flow within a microfluidic channel [35]. This means that

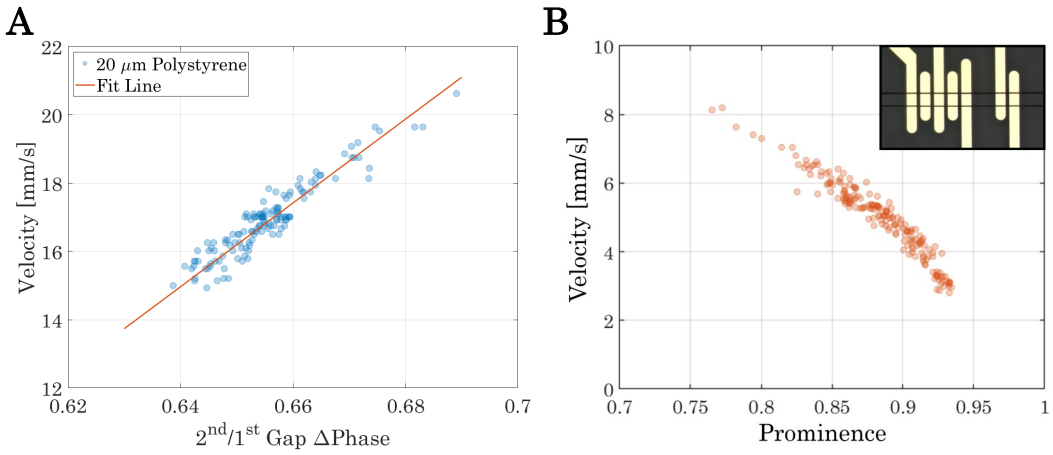

Figure 3.31: Correlation between the peak ratios and particle velocity shown with A) Double microwave gap design and B) Five-electrode design.

the fluid's velocity is highest at the center of the channel and gradually decreases as it approaches the channel's walls. Consequently, microparticles moving within this fluid experience a diverse range of velocities based on their position within the channel.

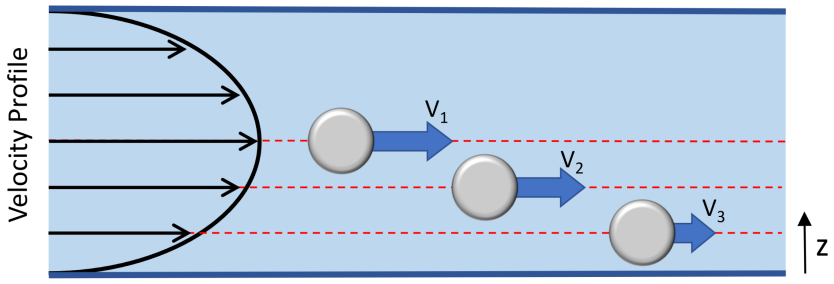

Figure 3.32: Effect of parabolic fluid velocity profile in a microchannel on particle velocity as a function of vertical position

Microparticles closer to the bottom wall of the channel tend to move at a slower pace due to the drag exerted by the channel surface. This phenomenon is especially dominant when working with particles near the micrometer scale. Their motion is strongly influenced by the proximity to the wall, leading to reduced velocities and often resulting in a concentration of particles near the bottom surface. Conversely, microparticles that reside closer to the channel's centerline

experience higher velocities. The fluid at this location moves faster, transferring greater momentum to particles positioned here. As a result, these particles are often observed to move more swiftly through the channel.

The results of this device are explained in the Experimental Results section.

Chapter 4

Experimental Results

Understanding the dielectric properties and geometrical characteristics of micro-scale particles and cells has profound implications across various scientific domains, from materials science to biomedicine. In this chapter, we present the outcomes of a series of experiments conducted using the latest version of the sensor developed for the precise measurement of dielectric permittivity and geometrical size of microparticles and cells. These experiments explore the realms of distinguishing between particles and analyzing cells, providing insights into various aspects of the behavior and characteristics of micro-scale particles and cells.

The chapter is divided into four sections, each dedicated to a unique experiment. In the first section, "Differentiation of Different Size Polystyrene Microparticles," we explore the sensor's capabilities in discerning between particles of varying sizes. The second section, "Differentiation of Polystyrene and Soda Lime Glass Microparticles," extends our inquiry to distinguish particles of different material compositions, providing insight into the sensor's versatility.

Moving beyond particle differentiation, the third section, "Effect of Cell Fixing," delves into the intriguing world of cellular analysis. Here, we investigate

the impact of cell fixation on dielectric permittivity and size measurements, unraveling the complexities of cell behavior when subjected to fixation processes.

The findings of these experiments not only broaden our understanding of micro-scale entities but also highlight the potential applications of our specialized sensor technology in various research areas.

4.1 Differentiation of Different Size Polystyrene Microparticles

In this section, we conduct a series of experiments with the aim of addressing some fundamental questions regarding the performance and capabilities of the sensor. These questions include understanding how the sensor reacts to particles of varying sizes, exploring the potential of the out-of-phase component, and gaining insight into the nature of our measurements.

To tackle these key inquiries, we begin our experimentation with an examination of high-precision polystyrene particles, specifically those measuring 10 and 20 μms in diameter. These particles are chosen for their well-defined characteristics, making them ideal candidates for studying the sensor's response and behavior.

In this control experiment, a diluted concentration was intentionally used to minimize potential errors arising from the passage of multiple particles. Over a 10-minute duration, we conducted measurements on a total of 315 microparticles successfully. Figure 4.1 illustrates the processed microwave phase (θ) and impedance cytometry voltage (ΔV) signals, featuring a magnified inset that distinctly displays the formation of double peaks for one 10, one 20 μm particle. On a broader scale, the smaller peaks correspond to 10 μm particles, while the larger ones represent 20 μm particles. It is worth noting that, due to the shorter measurement duration of microwave signals compared to impedance cytometry, a higher occurrence of multi-event passages is naturally observed in the low-frequency signal. Figure 4.1B showcases three instances of multi-particle passages

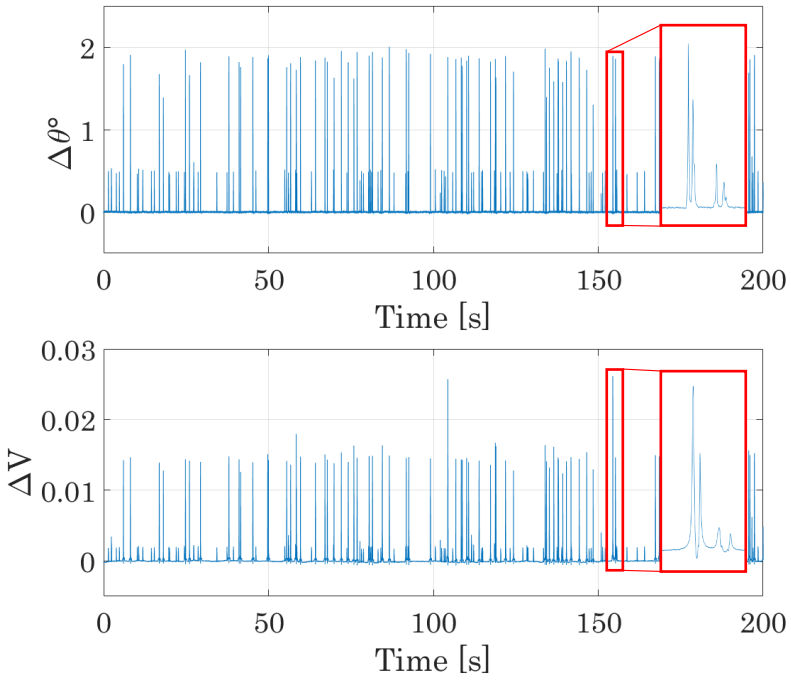

Figure 4.1: Processed data of a mix solution of 10 and 20 μm calibration particles. A) Microwave phase change B) Impedance cytometry Voltage change

at seconds 58 (10 & 20), 104 (20 & 20), and 155 (20 & 20) while they are distinct in the phase signal. Given that low-frequency signals can be superimposed by a basic summation, their identification and exclusion become straightforward when utilizing calibration particles exclusively.

As anticipated by the fundamental nature of resistance, Equation XXX, it is only logical for the low-frequency signal to be proportional to the geometrical volume of the particles. 20 μm particles induce 8 times larger values than 10 μm ones do. Therefore, with a basic cube root calculation, the size fits perfectly to the geometrical diameter representer value, the cube root of Impedance cytometry signal ($IC^{1/3}$)

The change in capacitance resulting from immersing a dielectric particle in another dielectric medium under the influence of an electric field can be determined by using the Clausius-Mossotti factor in Equation [19, 20]. According to these equations, ΔC is a function that depends on the third power of the particle

radius and is directly proportional to the out-of-phase component. Therefore, the cube root of the out-of-phase component should be related to the radius of particles with the same material content. However, we observed a discrepancy in the out-of-phase component (ΔY) in our experimental results. Contrary to our expectations, the square root of the out-of-phase component consistently showed a proportional relationship with the particle radius, as illustrated in Figure 3. The fitted line closely aligns with the clusters of data points.

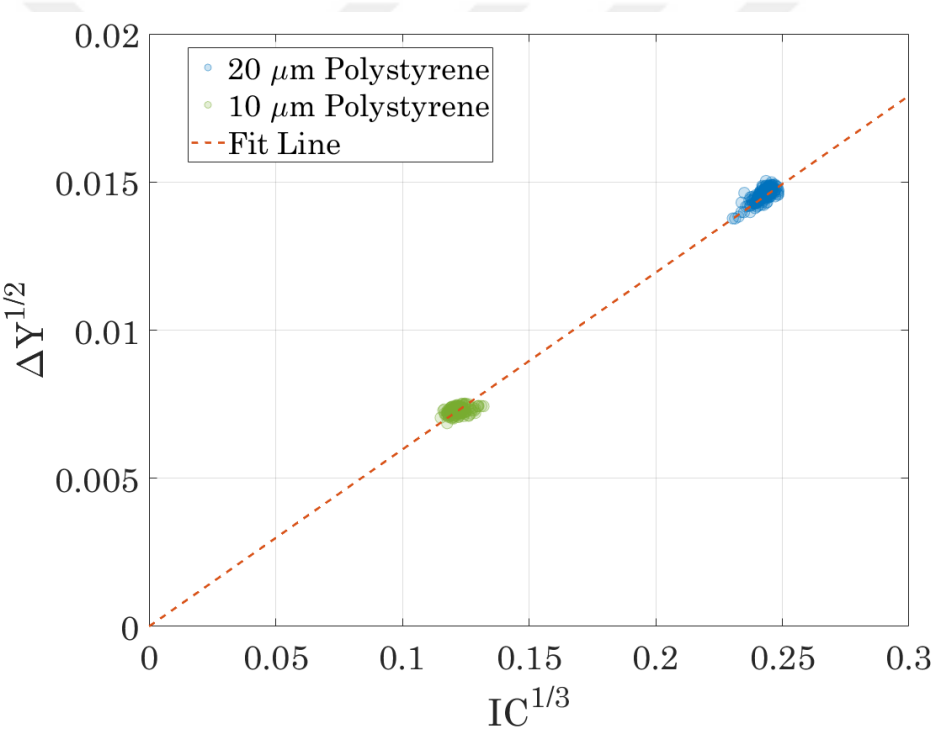

Figure 4.2: Results of the 10 and 20 μm polystyrene measurement.

We have not yet determined the exact reason for this contradiction, but it may be linked to the non-uniform formation of the electric field between the coplanar electrodes. Since the entire volume of a particle does not experience the same strength of the electric field, each differential volume affecting the change in capacitance is influenced differently. Since the signal is radiating from the bottom of the microchannel, the lower part of the particle experiences a stronger electric field, while the upper part experiences a weaker electric field. This hypothesis is supported by similar measurements conducted in a recent study that used a 3D structure to create a uniform electric field between the microwave electrodes [36].

In this study, the particle radius was found to be proportional to ($\Delta Y^{0.4}$) which is a closer value to the cube root.

4.2 Differentiation of Polystyrene and Soda Lime Glass Microparticles

In this experiment, we conducted a comparison between two types of microparticles: polystyrene and soda lime glass. We utilized the wide range of sizes found in the soda lime glass particles (Cospheric SLGMS-2.5 with a size distribution ranging from 15 to 22 μm) to validate a scaling relationship between impedance cytometry and microwave measurements. This validation was achieved by plotting the data on a logarithmic scale (log-log plot), as depicted in Figure 4.3A.

The slope of the log-log plot was calculated to be 0.646 $\pm$ 0.014, which is approximately 2/3. This slope indicated that the microwave signal scaled with the square of the diameter, while the impedance cytometry signal scaled with the cube of the diameter. This ratio of 2/3 closely matched the results observed in the previous experiment.

Moving forward in Figure 4.3, both the soda lime glass particles (in blue) and the polystyrene particles (in orange) with a narrower diameter distribution (20$\pm$0.3 μm) were included. According to the observed scaling trend, the slope on this chart is directly related to the square root of the $|K_{CM}|$ value for each particle. Figure 4B clearly shows the distinction in slopes between the two particle types. As anticipated, polystyrene particles exhibited higher K_{CM} values, reflected in their steeper slope compared to soda lime glass (with K_{CM} factors of -0.47 for polystyrene and -0.43 for soda lime glass, respectively). The inset in Figure 4B illustrates the separation boundary between polystyrene and soda lime glass. In a binary separation scenario, the technique demonstrated an overall accuracy of 94.9% when two particles were sequentially introduced into the system.

Figure 4.3C presents the absolute values of the K_{CM} factors for the particles at

microwave frequencies. The results suggest that polystyrene beads obstruct the penetration of the electrical field, as expected due to their differing permittivity compared to water. Calibration of the sensor response using the known K_{CM} factor of polystyrene resulted in values of 0.47 (σ = 5.5 x $10^{-}3$) for polystyrene and 0.43 (σ = 1.4 x $10^{-}2$) for soda lime glass. These values aligned with the expected ratio.

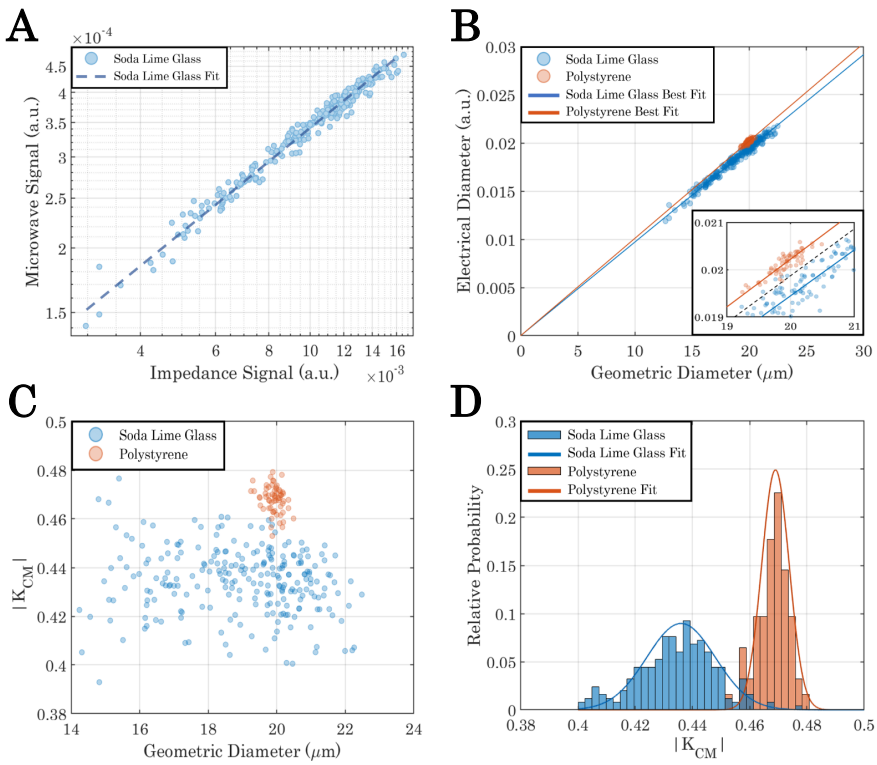

Figure 4.3: (A) The velocity-calibrated signals from impedance cytometry (x-axis) and microwave sensors (y-axis) of soda lime glass particles on a logarithmic scale. (B) Separation of polystyrene and soda lime glass using geometric and electrical diameters. (C) Separation by the $|K_{CM}|$ factor of polystyrene and soda lime glass (D) Histogram of $|K_{CM}|$ factor showing material classification along with separating Gaussian fits.

In Figure 4.3D, the histogram demonstrates that differences in the Clausius-Mossotti factor can be utilized for classifying various dielectric materials. Furthermore, by focusing solely on the polystyrene group (characterized by a narrow size distribution), we determined the technique's resolution. Both geometric and electrical diameter measurements yielded a standard deviation-to-mean ratio of

1.2%. This high resolution in individual parameters translated to a narrow distribution of their ratio, which, in turn, allowed the differentiation of two materials with very similar dielectric properties.

Material	Number of Particles	Number of Misclassifications	Successful Separation (%)
Polystyrene	62	2	96.8
Soda Lime Glass	249	14	94.4
Total	311	16	94.9

Figure 4.4: Statistical results of the polystyrene and soda-lime glass experiment

By assessing these microparticles as material-specific groups, the sensor effectively demonstrated its ability to distinguish polystyrene and soda lime glass microparticles based on their dielectric permittivity, achieving a 94% accuracy rate.

4.3 Effect of Cell Fixing

In addition to the differentiation of microparticles based on their dielectric properties, our research extended to the analysis of individual cells, showcasing the potential applications in biomaterials and bioelectronics. The ability to non-invasively investigate and differentiate the internal composition of single cells provides valuable insights into cellular physiology, behavior, and responses to various stimuli.

Specifically, in this experiment, our focus was on assessing the impact of cell fixation, employing glutaraldehyde, on MDA-MB-231 cells. The fixation process serves to preserve the structural and biochemical attributes of cells while cross-linking their proteins and nucleic acids. This effect is particularly pronounced with glutaraldehyde, a widely-used substance in the preparation of biological samples for electron microscopy due to its proficiency in preserving cellular shape. Although the fixation process maintains cell volume and structure, it modifies

their inherent material composition. As anticipated from our biochemical observations, the low-frequency sensor recorded similar cellular volumes, while the microwave sensor demonstrated distinct changes in internal material properties (Figure 4.5A). Calibration during both runs involved the use of polystyrene particles.

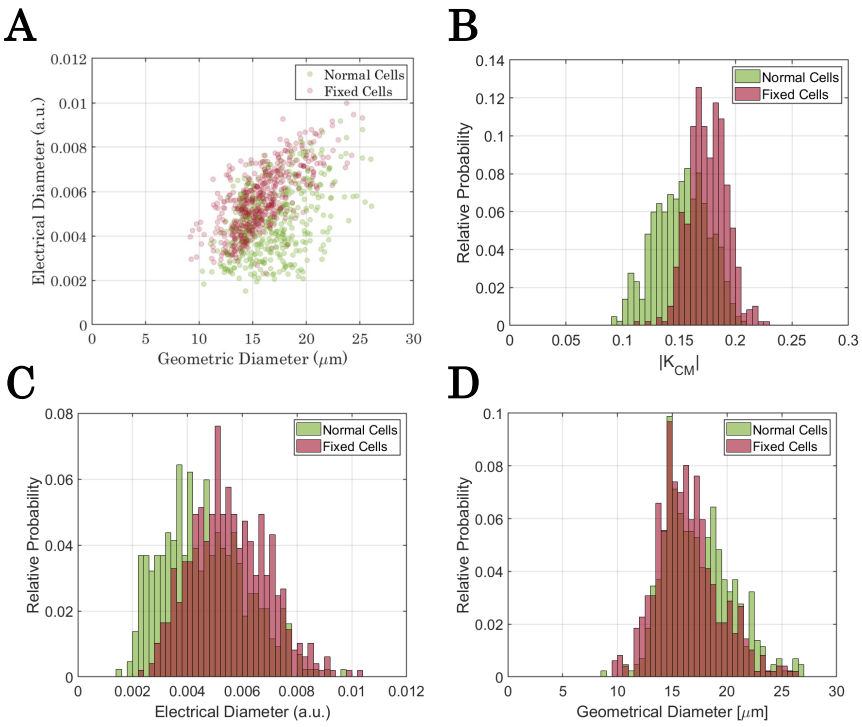

Figure 4.5: (A) Demonstration of the effect of fixing MDA-MB–231 Cells on their geometric and electrical diameter by measuring cells before and after the procedure. (B) $|K_{CM}|$ distribution before (mean:0.151) and after (mean:0.178) the fixation. C) Electrical diameter of cells before and after the fixing procedure. D) Geometrical diameter of cells before and after the fixing procedure.

Subsequent to fixation, the mean (initial: 17.3 μm, post-fixation: 16.9 μm) and standard deviation (initial: 3.1 μm, post-fixation: 2.8 μm) of impedance cytometry signals remained unaltered (Figure 4.5D), affirming the preservation of cell volume and structure. In contrast, the microwave signal, indicative of cell permittivity, exhibited a 24% increase (initial: 0.0045, post-fixation: 0.0056), signaling a decrease in the dielectric permittivity of the internal material of cells (Figure 4.5C). Remarkably, the distribution of $|K_{CM}|$, as represented by the square

of the ratio of electrical diameter to geometrical diameter, validated the potential of this technique for single-cell analysis, offering insights into the internal state of cells (Figure 4.5B).

These findings further support the intriguing possibilities for the application of our sensor technology in cellular analysis. The sensor's ability to discern slight yet crucial changes in electrical properties, even while the geometrical size remains consistent, is a valuable asset. This capability enables us to gain deeper insights into how cells react to external agents over time.

Chapter 5

Methodology

Of course, you may increase or decrease the number of chapters as appropriate to your thesis.

5.1 Fabrication

The sensor device was fabricated on one half of a 100 mm x 0.5 mm (diameter x thickness) double-side polished wafer. The substrate was chosen to be dry-fused quartz, a non-conductive and low-loss-tangent material. Sensor geometry was patterned by spin coating 2 µm thick AZ – 5214 photoresist and photolithography steps. After the photoresist development in AZ – 400K for 30 seconds, 5 nm of chromium and 150 nm of gold were deposited by the thermal evaporation process. Chromium was used as a binding agent between quartz and gold layers. After an overnight acetone lift-off process, the sensor pattern was completed. For the microchannel fabrication, the SU-8 mold was used to create channel patterns on a PDMS block. After punching the fluidic inlet and outlet through the PDMS block, the bottom surface of the channel and the gold-deposited wafer were treated with oxygen plasma to activate their surfaces. Within ten minutes after the activation, the microfluidic channel and the wafer were aligned and bounded under an optic

microscope. The details of the fabrication process are explained in the following series of videos step by step:

Dicing saw process: `https://youtu.be/ITO7Wos05eQ`

Spin Coating: `https://youtu.be/Migmv8Cl8aQ`

Photolithography: `https://youtu.be/1U_EjhYCrEw`

Metal deposition: `https://youtu.be/T7s-cgiXN-I`, `https://youtu.be/8oM4d3qli9E`, `https://youtu.be/kBuLBXMPvFI`

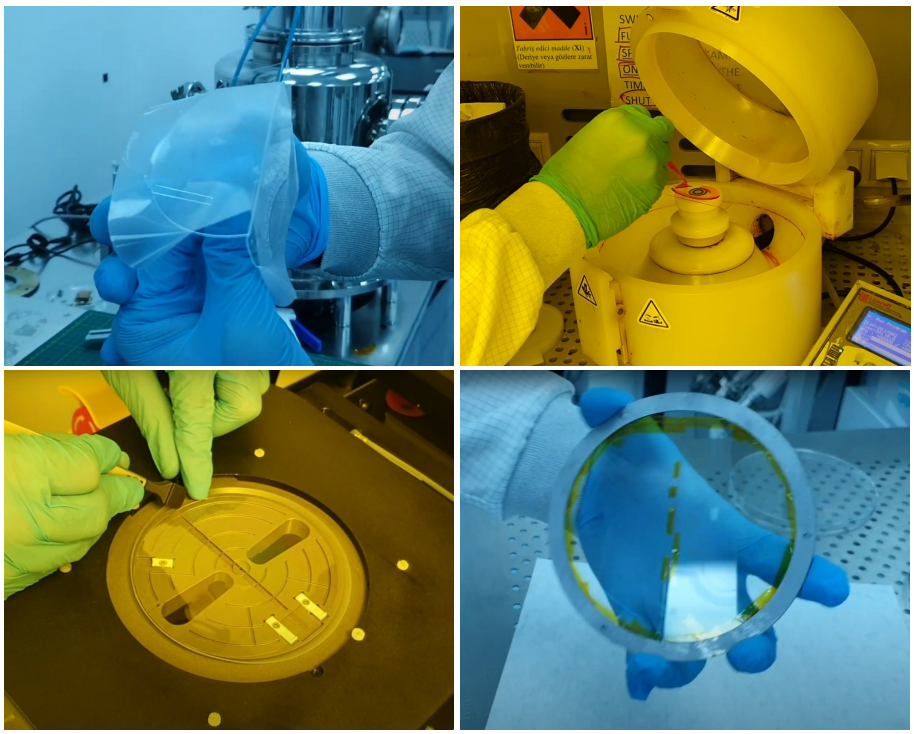

Figure 5.1: A) Removal of the cut fused silica wafer from the dicing saw tape. B) Placement of photoresist before the spin coating process. C) Alignment of wafers in the photolithography device. D) Preparation of wafers for insertion into the thermal evaporator device. Sections with limited photoresist coverage are protected by Kapton tape to prevent unintended metal deposition.

5.2 Experimental Setup

The experimental setup has been carefully isolated to minimize the influence of environmental factors and ensure precise measurements. The sensor platform is positioned on an optical table to mitigate the impact of physical vibrations. This setup is further enclosed within a transparent plastic casing, effectively restraining temperature fluctuations and preventing disruptive airflow caused by ventilation systems. Surrounding this protective casing, a Faraday cage has been installed to shield against environmental interferences, including any accidental disturbances within the laboratory. This is particularly crucial because the resonating sensor functions as an extremely sensitive antenna, and even the slightest movements by the operator can introduce unwanted noise into the sensor readings.

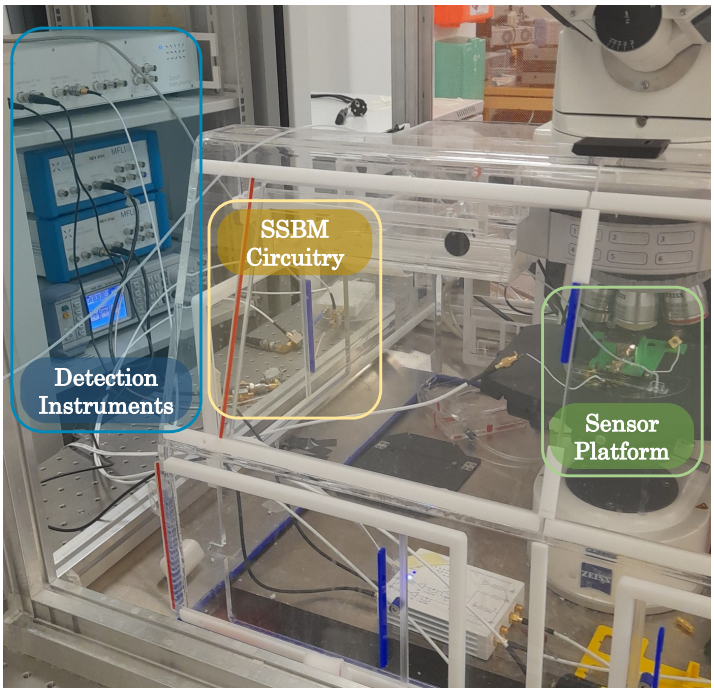

Figure 5.2: Experimental setup

The sensor itself is mounted on a 3D-printed holder, which can be attached to a microscope tray for precise positioning. Electrical instruments are placed on a rack located outside the Faraday cage to avoid any electromagnetic interference.

For the microwave measurements, we employ two MFLI lock-in amplifiers and a Rohde Schwarz signal generator to establish Single-Sideband Modulation (SSBM) circuitry. One of the lock-in amplifiers serves as the 'leader,' while the other functions as the 'follower.' Through synchronization facilitated by a clock signal modulated from the leader, these amplifiers are finely tuned to generate signals with a 90-degree phase difference at kHz frequencies, providing in-phase and quadrature components for SSBM. Subsequently, these signals are upconverted in the IQ-mixer, which is driven by the GHz frequency signal supplied by the signal generator through the Local Oscillator (LO) port. This process yields a signal at the difference frequency of LO and the lock-in output frequency.

This signal is then directed to the Device Under Test (DUT) via a circulator, a specialized microwave component that routes signals based on their incoming direction. The reflected voltage wave reaches a second mixer, where it undergoes down-conversion to the lock-in frequencies, facilitating dual-phase demodulation. Finally, the follower lock-in amplifier extracts the R (magnitude) and θ (phase) values (as depicted in Figure 5.3).

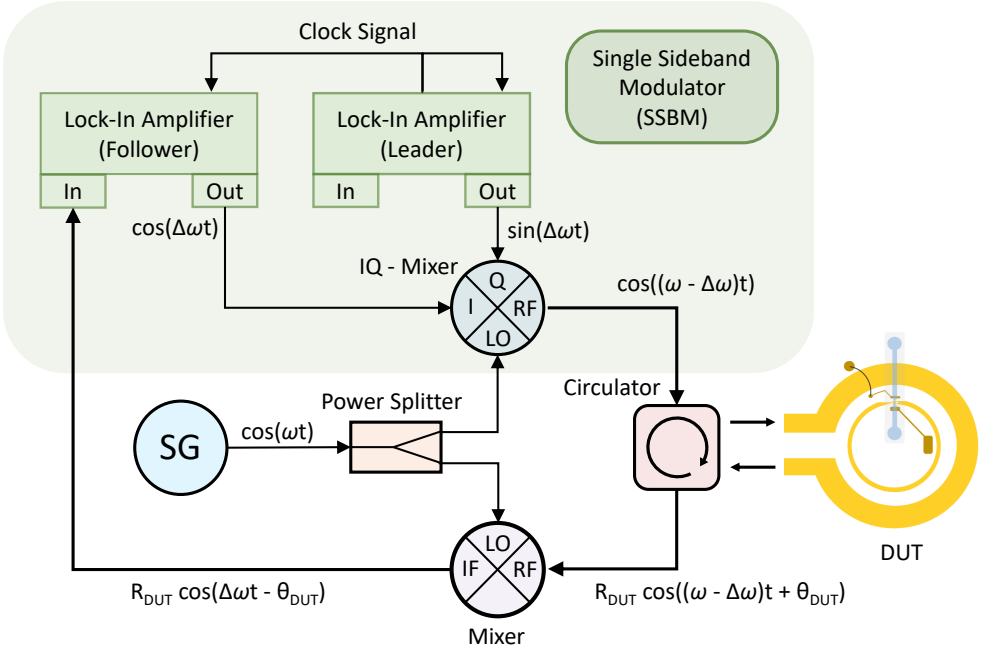

Figure 5.3: Detailed microwave circuitry.

Fluid control is adjusted through the Fluigent MFCS-EZ microfluidic flow

control system. To introduce micro-objects to the sensor, a droplet of solution is carefully deposited onto the microfluidic outlet of the sensor (Visible on the left end of the PDMS block in Figure 5.4). Subsequently, negative pressure is applied for a few minutes to draw the solution into the channel. Once an adequate volume of solution is loaded into the sensor, any remaining droplets are carefully removed using a tissue without touching the sensor. The experimental process is initiated by introducing positive pressure into the microfluidic channel, thus pushing the loaded particles through the sensing region.

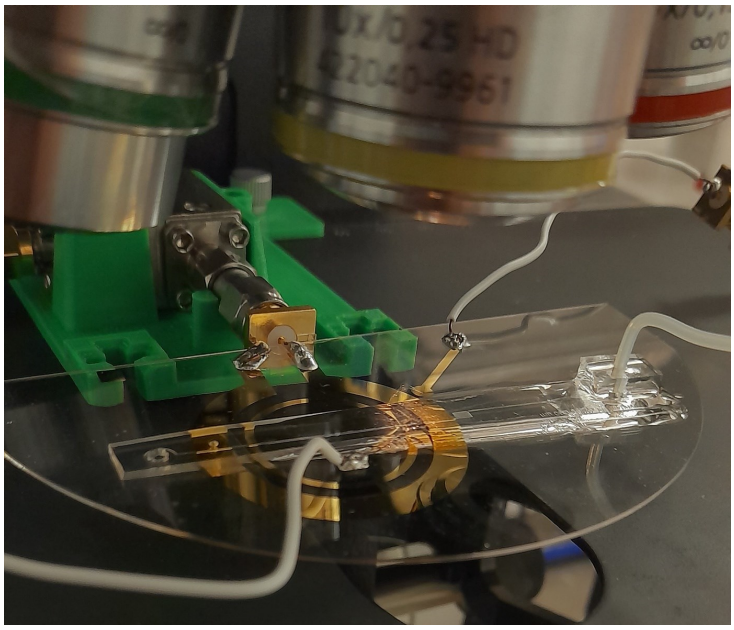

Figure 5.4: Close-up view of the sensor with all the electrical and fluidic connections.

This approach of introducing the solution from the outlet offers two significant advantages. First, it necessitates fewer movements, reducing the likelihood of inadvertently altering the sensor's position, which could otherwise compromise the integrity of the experiment by affecting resonance characteristics. Second, it enables the introduction of denser particles, such as soda-lime glass ($\rho = 2.5g/cm^3$), which are typically challenging to utilize within microtubing systems.

5.3 Experimental Procedure

To initiate the experiment, we load the solution of interest into the sensor and perform a frequency sweep using our circuitry. Given the inherent slight variations in resonance frequency between individually fabricated sensors, our sweep encompasses a range from 4.6 to 5.8 GHz to precisely identify the resonance frequency.

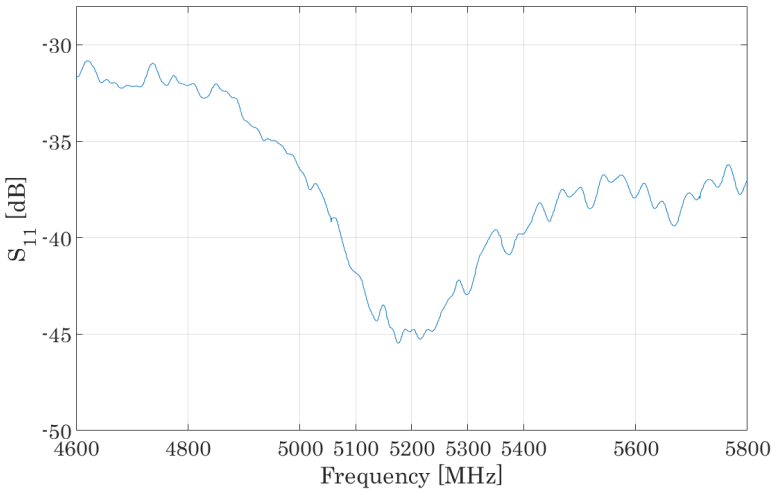

Figure 5.5: Amplitude response of the sensor to frequency sweep.

The frequency at which the reflected voltage from the device reaches its minimum is considered the resonance frequency. In an illustrative example (Figure X1), this frequency falls within the range of 5.1 to 5.3 GHz. Nevertheless, even within this narrow range, the sensor's response exhibits considerable variability.

To identify the most sensitive frequency, we conduct a secondary sweep by incrementally adjusting the signal generator frequency in 10 MHz steps. During this optimization process, the sensing region is observed under a microscope, and a calibration particle—typically a 20 μm polystyrene particle—is introduced into the region using controlled flow. At each frequency step, the particle is passed back and forth through the sensing region once.

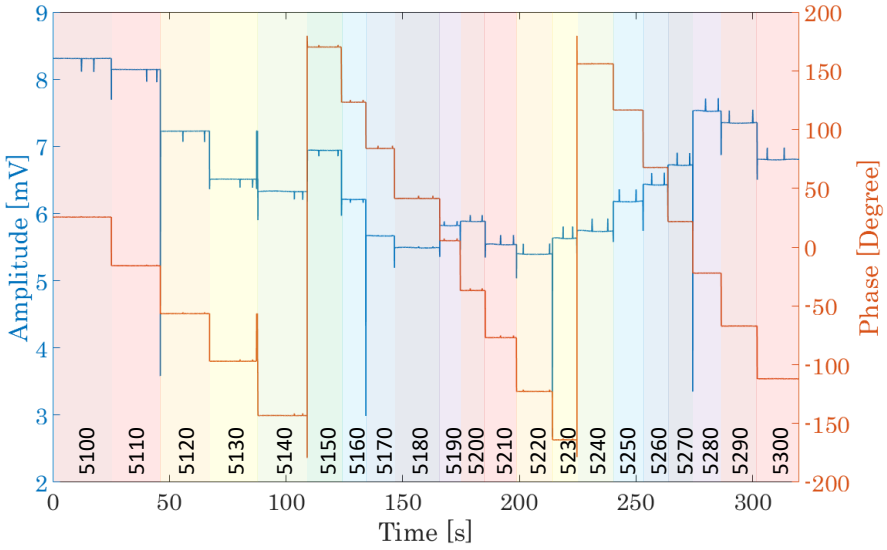

Figure 5.6: The data of the resonance frequency optimization experiment.

The response of the microwave parameters varies notably throughout this frequency sweep, even undergoing sign changes, as depicted in Figure X2. Since frequency steps add up to a large change in phase value, the change values are more clear in Figure X3.

To obtain the highest quality out-of-phase component, we select a frequency that maximizes the signal-to-noise ratio (SNR) for both amplitude and phase. This entails dividing the signal values displayed in Figure X3 by the standard deviation of the noise at each frequency, resulting in the table presented in Figure X4.

In this specific instance, the optimal resonance frequency for particle detection was determined to be 5230 MHz, with an SNR of 1594 for amplitude and 822 for phase measurement. Subsequently, following the selection of the best resonance frequency, we initiate data acquisition and allow particles or cells to pass through the sensing region.

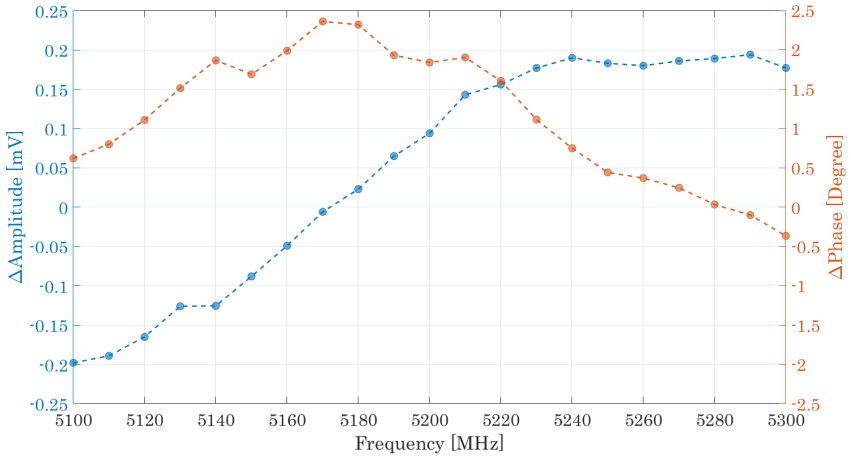

Figure 5.7: Amplitude and phase response to 20 μm polystyrene particle for each 10 MHz frequency step

Frequency	5100	5110	5120	5130	5140	5150	5160	5170	5180	5190	5200
Δ Amp	-0.198	-0.189	-0.165	-0.126	-0.122	-0.088	-0.049	-0.006	0.023	0.065	0.094
SNR Amp	763	653	1073	642	644	456	280	42	146	395	660
Δ Phase	0.618	0.798	1.106	1.51	1.863	1.686	1.985	2.358	2.316	1.928	1.836
SNR Phase	145	597	448	1162	751	989	1380	1672	1563	1433	1167

Frequency	5210	5220	5230	5240	5250	5260	5270	5280	5290	5300	
Δ Amp	0.143	0.156	0.177	0.19	0.183	0.18	0.186	0.189	0.194	0.177	
SNR Amp	1256	1311	1594	1648	1324	1102	1116	1037	1096	1151	
Δ Phase	1.9	1.602	1.111	0.746	0.44	0.367	0.244	0.032	-0.101	-0.367	
SNR Phase	980	973	822	605	340	215	132	24	68	261	

Figure 5.8: Signal to noise ratio of amplitude and phase response for each 10 MHz frequency step

5.4 Data Analysis

In this section, only the final version of the data analysis is explained. The data from the microwave and impedance cytometry sensors are collected simultaneously using lock-in amplifiers, specifically MFLI and HF2LI. To ensure the capture of at least 200 data points per event, a sampling rate of >10kSamp/sec is selected for both instruments. The closest available sampling rates are chosen, resulting in 13.392 kSamp/sec for the MFLI and 14.391 kSamp/sec for the HF2LI. To align the number of data points, MATLAB's Signal Processing Toolbox is utilized, employing the 'resample' function to resample each dataset.

Subsequently, by selecting event data belonging to the same particle from both

the microwave and impedance cytometry signals, the time delay between the two measurements is calculated and synchronized accordingly. However, it is important to note that the fluid medium used, Phosphate-buffered saline (PBS), is not perfectly homogeneous, leading to signal drift during the experiments. To improve the accuracy of capturing event magnitudes, MATLAB's Bioinformatics Toolbox is employed, utilizing the 'msbackadj' function to remove the drift effect. For the microwave data, the baseline is subtracted, while for the impedance cytometry data, the data points are normalized by dividing them by the baseline values, as the current blockage is proportional to its baseline.

In our analysis, we employ a two-step convolution process to identify events involving single and multiple particle passages. To illustrate this, consider the time-domain phase data of three events in Figure 5.9. In this example, the third event is well-isolated, while the first two events are closely spaced, making their characterization less reliable. In the initial convolution operation, the first two events yield two distinct peak pairs with varying shapes, while the third event results in a symmetric pair. Subsequently, after the second convolution operation, which involves Gaussian smoothing, the first two events merge into a multi-peak shape. Following this, we employ a standard MATLAB peak finder algorithm to detect all peaks. If there is no value smaller than a predefined threshold between two adjacent peaks, they are categorized as multiple-event passages. In this specific scenario, events occurring within a time interval of less than 40 ms (which is contingent on the convolution window length) are considered as multiple-event passages and are subsequently excluded from the analysis.

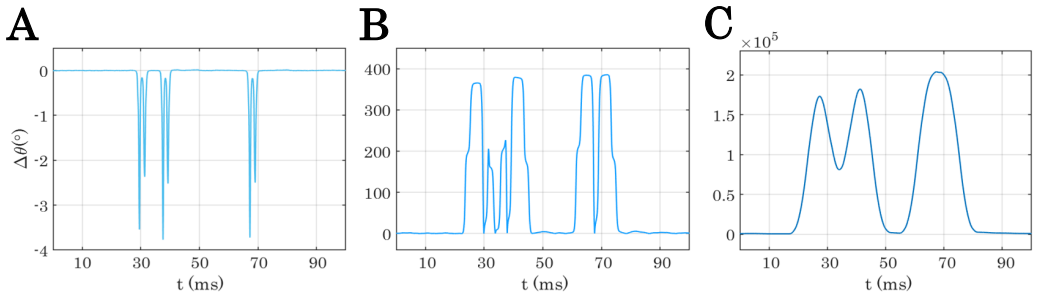

Figure 5.9: A)Raw data. B) First and C) second stage of convolution.

Valid event values are identified using the built-in 'findpeaks' function in MATLAB. By calibrating the impedance cytometry amplitude, microwave amplitude, and phase values, the diminishing effect of the particle height is eliminated. By leveraging the known geometric value of polystyrene, the electrical signal from the impedance cytometry data is transformed into μm units by multiplying it by a constant value, and the electrical diameter of the particles is calculated using the ΔY quadrature formula. While the convolution step successfully excludes most multi-particle passages, it is possible for microparticles to adhere together and be measured as groups. To address this, additional filters are implemented. In the first filter, the dielectric permittivity values of the final data points are computed, and any data point falling outside the 5 standard deviations range from its mean is excluded for each microparticle type. The second filter specifically targets soda lime glass microparticle events, removing those with sizes below 12 μm or above 25 μm as they are out of the size range provided by the vendor.

Chapter 6

Conclusion and Future Work

This thesis introduces a portable, rapid, and cost-effective chip-sized solution for the analysis of micron-level objects. The sensor developed in this work has the capability to differentiate between two distinct classes of dielectric microparticles, even when they share similar electronic characteristics. Additionally, it can measure internal changes in cells resulting from specific treatments.

To achieve this differentiation capability, we integrated two electronic sensors operating at significantly different frequencies: a 500 kHz sensor for geometric sizing and a microwave sensor at approximately 5 GHz for electrical sizing. By combining the data from these two sensors, we derived intrinsic material properties for each microparticle, achieving an impressive identification accuracy of 94.9% in distinguishing between polystyrene and glass microparticles. Notably, our sensor offers a substantially faster analysis speed, with particles spending only 25 milliseconds in the sensing region. This speed holds great potential for automating microparticle analysis in environmental and materials science applications.

Furthermore, our sensor design exhibited the ability to differentiate between healthy and fixed cells. This feature has significant implications for biomedical research, offering a less invasive alternative to current methods that rely on

complex measurements of refractive indices or fluorescent labeling.

However, it's important to acknowledge some limitations. Our current approach is primarily suited for the classification of materials with distinct dielectric permittivity values. Enhancing sensor resolution could expand its applicability to a wider range of material classes, benefiting materials and environmental sciences. Moreover, using a medium with lower permittivity than water could enhance signal contrast for different microparticle materials, and further research can explore this potential.

In conclusion, our findings hold immense promise. The ability to differentiate microparticles among various material classes in water has applications ranging from environmental pollutant identification to manufacturing quality control and the capability to analyze cells' internal content holds significant promise in advancing our comprehension of cellular mechanisms, enabling more precise characterization of cell types, and facilitating the development of personalized diagnostics and therapies.

Bibliography

[1] J. Schneider, C. A. Browne, M. Slutzky, C. A. Quirk, D. B. Amchin, and S. S. Datta, "Fluid drainage in erodible porous media," *arXiv preprint arXiv:2303.01260*, 2023.

[2] X. Lim *et al.*, "Microplastics are everywhere—but are they harmful," *Nature*, vol. 593, no. 7857, pp. 22–25, 2021.

[3] S. Nagrath, L. V. Sequist, S. Maheswaran, D. W. Bell, D. Irimia, L. Ulkus, M. R. Smith, E. L. Kwak, S. Digumarthy, A. Muzikansky, *et al.*, "Isolation of rare circulating tumour cells in cancer patients by microchip technology," *Nature*, vol. 450, no. 7173, pp. 1235–1239, 2007.

[4] D. C. Spencer, T. F. Paton, K. T. Mulroney, T. J. Inglis, J. M. Sutton, and H. Morgan, "A fast impedance-based antimicrobial susceptibility test," *Nature communications*, vol. 11, no. 1, p. 5328, 2020.

[5] E. Lagreca, V. Onesto, C. Di Natale, S. La Manna, P. A. Netti, and R. Vecchione, "Recent advances in the formulation of plga microparticles for controlled drug delivery," *Progress in biomaterials*, vol. 9, pp. 153–174, 2020.

[6] M. G. Blevins, H. L. Allen, B. C. Colson, A.-M. Cook, A. Z. Greenbaum, S. S. Hemami, J. Hollmann, E. Kim, A. A. LaRocca, K. A. Markoski, *et al.*, "Field-portable microplastic sensing in aqueous environments: A perspective on emerging techniques," *Sensors*, vol. 21, no. 10, p. 3532, 2021.

[7] H. De Frond, L. T. Hampton, S. Kotar, K. Gesulga, C. Matuch, W. Lao, S. B. Weisberg, C. S. Wong, and C. M. Rochman, "Monitoring microplastics

in drinking water: An interlaboratory study to inform effective methods for quantifying and characterizing microplastics," *Chemosphere*, vol. 298, p. 134282, 2022.

[8] J. C. Prata, J. P. da Costa, I. Lopes, A. C. Duarte, and T. Rocha-Santos, "Environmental exposure to microplastics: An overview on possible human health effects," *Science of the total environment*, vol. 702, p. 134455, 2020.

[9] S. Gawad, L. Schild, and P. Renaud, "Micromachined impedance spectroscopy flow cytometer for cell analysis and particle sizing," *Lab on a Chip*, vol. 1, no. 1, pp. 76–82, 2001.

[10] A. Fazelkhah, S. Afshar, N. Durham, M. Butler, E. Salimi, G. Bridges, and D. Thomson, "Parallel single-cell optical transit dielectrophoresis cytometer," *Electrophoresis*, vol. 41, no. 9, pp. 720–728, 2020.

[11] R. Goldston and P. Rutherford, "Introduction to plasma physics institute of physics," 1997.

[12] J. Picot, C. L. Guerin, C. Le Van Kim, and C. M. Boulanger, "Flow cytometry: retrospective, fundamentals and recent instrumentation," *Cytotechnology*, vol. 64, pp. 109–130, 2012.

[13] D. J. Rowe, S. Al-Malki, A. A. Abduljabar, A. Porch, D. A. Barrow, and C. J. Allender, "Improved split-ring resonator for microfluidic sensing," *IEEE Transactions on microwave theory and techniques*, vol. 62, no. 3, pp. 689–699, 2014.

[14] T. Chen, F. Artis, D. Dubuc, J. Fournie, M. Poupot, and K. Grenier, "Microwave biosensor dedicated to the dielectric spectroscopy of a single alive biological cell in its culture medium," in *2013 IEEE MTT-S International Microwave Symposium Digest (MTT)*, pp. 1–4, IEEE, 2013.

[15] C. Dalmay, M. Cheray, A. Pothier, F. Lalloué, M. Jauberteau, and P. Blondy, "Ultra sensitive biosensor based on impedance spectroscopy at microwave frequencies for cell scale analysis," *Sensors and Actuators A: Physical*, vol. 162, no. 2, pp. 189–197, 2010.

[16] Y. Yang, H. Zhang, J. Zhu, G. Wang, T.-R. Tzeng, X. Xuan, K. Huang, and P. Wang, "Distinguishing the viability of a single yeast cell with an ultra-sensitive radio frequency sensor," *Lab on a Chip*, vol. 10, no. 5, pp. 553–555, 2010.

[17] M. Kelleci, H. Aydogmus, L. Aslanbas, S. O. Erbil, and M. S. Hanay, "Towards microwave imaging of cells," *Lab on a Chip*, vol. 18, no. 3, pp. 463–472, 2018.

[18] S. Afshar, E. Salimi, K. Braasch, M. Butler, D. J. Thomson, and G. E. Bridges, "Multi-frequency dep cytometer employing a microwave sensor for dielectric analysis of single cells," *IEEE Transactions on Microwave Theory and Techniques*, vol. 64, no. 3, pp. 991–998, 2016.

[19] G. A. Ferrier, S. F. Romanuik, D. J. Thomson, G. E. Bridges, and M. R. Freeman, "A microwave interferometric system for simultaneous actuation and detection of single biological cells," *Lab on a Chip*, vol. 9, no. 23, pp. 3406–3412, 2009.

[20] M. Nikolic-Jaric, S. Romanuik, G. Ferrier, G. Bridges, M. Butler, K. Sunley, D. Thomson, and M. Freeman, "Microwave frequency sensor for detection of biological cells in microfluidic channels," *Biomicrofluidics*, vol. 3, no. 3, 2009.

[21] J.-C. Chien, A. Ameri, E.-C. Yeh, A. N. Killilea, M. Anwar, and A. M. Niknejad, "A high-throughput flow cytometry-on-a-cmos platform for single-cell dielectric spectroscopy at microwave frequencies," *Lab on a Chip*, vol. 18, no. 14, pp. 2065–2076, 2018.

[22] F. Caselli and P. Bisegna, "A simple and robust event-detection algorithm for single-cell impedance cytometry," *IEEE Transactions on Biomedical Engineering*, vol. 63, no. 2, pp. 415–422, 2015.

[23] C. Laborde, F. Pittino, H. Verhoeven, S. Lemay, L. Selmi, M. Jongsma, and F. Widdershoven, "Real-time imaging of microparticles and living cells with cmos nanocapacitor arrays," *Nature nanotechnology*, vol. 10, no. 9, pp. 791–795, 2015.

[24] U. Tefek, B. Sari, H. Z. Alhmoud, and M. S. Hanay, "Permittivity-based microparticle classification by the integration of impedance cytometry and microwave resonators," *Advanced Materials*, p. 2304072.

[25] D. Holmes and H. Morgan, "Single cell impedance cytometry for identification and counting of cd4 t-cells in human blood using impedance labels," *Analytical chemistry*, vol. 82, no. 4, pp. 1455–1461, 2010.

[26] Y.-S. Chen, C.-H. Huang, P.-C. Pai, J. Seo, and K. F. Lei, "A review on microfluidics-based impedance biosensors," *Biosensors*, vol. 13, no. 1, 2023.

[27] C. W. Shields Iv, C. D. Reyes, and G. P. López, "Microfluidic cell sorting: a review of the advances in the separation of cells from debulking to rare cell isolation," *Lab on a Chip*, vol. 15, no. 5, pp. 1230–1249, 2015.

[28] K. Cheung, S. Gawad, and P. Renaud, "Impedance spectroscopy flow cytometry: On-chip label-free cell differentiation," *Cytometry Part A*, vol. 65, no. 2, pp. 124–132, 2005.

[29] J. Zhong, M. Liang, and Y. Ai, "Submicron-precision particle characterization in microfluidic impedance cytometry with double differential electrodes," *Lab on a Chip*, vol. 21, no. 15, pp. 2869–2880, 2021.

[30] L. Collins, S. Jesse, J. I. Kilpatrick, A. Tselev, M. B. Okatan, S. V. Kalinin, and B. J. Rodriguez, "Kelvin probe force microscopy in liquid using electrochemical force microscopy," *Beilstein journal of nanotechnology*, vol. 6, no. 1, pp. 201–214, 2015.

[31] M. Z. Bazant, K. Thornton, and A. Ajdari, "Diffuse-charge dynamics in electrochemical systems," *Physical review E*, vol. 70, no. 2, p. 021506, 2004.

[32] A. Demir and M. S. Hanay, "Fundamental sensitivity limitations of nanomechanical resonant sensors due to thermomechanical noise," *IEEE Sensors Journal*, vol. 20, no. 4, pp. 1947–1961, 2019.

[33] A. De Ninno, V. Errico, F. R. Bertani, L. Businaro, P. Bisegna, and F. Caselli, "Coplanar electrode microfluidic chip enabling accurate sheathless impedance cytometry," *Lab on a Chip*, vol. 17, no. 6, pp. 1158–1166, 2017.

[34] D. Spencer and H. Morgan, "High-speed single-cell dielectric spectroscopy," *ACS sensors*, vol. 5, no. 2, pp. 423–430, 2020.

[35] J. M. Martel and M. Toner, "Inertial focusing in microfluidics," *Annual review of biomedical engineering*, vol. 16, pp. 371–396, 2014.

[36] Y. C. Alataş, U. Tefek, B. Sarı, and M. S. Hanay, "Microwave resonators enhanced with 3d liquid-metal electrodes for microparticle sensing in microfluidic applications," 2023.